CELL BIOLOGY

Specific mesoderm subset derived from human pluripotent stem cells ameliorates microvascular pathology in type 2 diabetic mice

Chang-Hyun Gil[1,2]†, Dibyendu Chakraborty[3]†, Cristiano P. Vieira[3], Nutan Prasain[1,4], Sergio Li Calzi[3], Seth D. Fortmann[3,5], Ping Hu[3], Kimihiko Banno[1,6], Mohamed Jamal[7,8], Chao Huang[3], Micheli S. Sielski[3], Yang Lin[1,9], Xinxin Huang[10,11], Mariana D. Dupont[3], Jason L. Floyd[3], Ram Prasad[3], Ana Leda F. Longhini[3,12], Trevor J. McGill[13], Hyung-Min Chung[14], Michael P. Murphy[2], Darrell N. Kotton[7], Michael E. Boulton[3], Mervin C. Yoder[1,15]*, Maria B. Grant[3]*

Human induced pluripotent stem cells (hiPSCs) were differentiated into a specific mesoderm subset characterized by KDR$^+$CD56$^+$APLNR$^+$ (KNA$^+$) expression. KNA$^+$ cells had high clonal proliferative potential and specification into endothelial colony-forming cell (ECFCs) phenotype. KNA$^+$ cells differentiated into perfused blood vessels when implanted subcutaneously into the flank of nonobese diabetic/severe combined immunodeficient mice and when injected into the vitreous of type 2 diabetic mice (*db/db* mice). Transcriptomic analysis showed that differentiation of hiPSCs derived from diabetics into KNA$^+$ cells was sufficient to change baseline differences in gene expression caused by the diabetic status and reprogram diabetic cells to a pattern similar to KNA$^+$ cells derived from nondiabetic hiPSCs. Proteomic array studies performed on retinas of *db/db* mice injected with either control or diabetic donor–derived KNA$^+$ cells showed correction of aberrant signaling in *db/db* retinas toward normal healthy retina. These data provide "proof of principle" that KNA$^+$ cells restore perfusion and correct vascular dysfunction in *db/db* mice.

INTRODUCTION

The ability to genetically reprogram patient somatic cells into human induced pluripotent stem cells (hiPSCs) has provided a new tool to model multifactorial diseases (*1*), allowing hiPSC-derived cells as potential therapeutic agents for damaged tissues and organs (*2*). Generation of hiPSC-derived endothelium has been proposed as a means to investigate basic mechanisms of vasculogenesis and angiogenesis both in health and disease (*3*). However, modeling the endothelial cell (EC) dysfunction, for example, as seen with diabetic microvascular disease has been challenging using hiPSCs (*1*). Despite these limitations, diminished angiogenic function has been observed in hiPSC-derived ECs from diabetic individuals (*4*). Whether this represents a true disease-related defect or is related to the protocol used to generate the cells is not known. Thus, the goal of this study was to generate hiPSCs from control and also diabetic individuals, develop a novel differentiation protocol, and examine the in vitro and in vivo function of EC precursors generated from hiPSCs.

We reasoned that the key to obtaining ECs from hiPSCs was to understand the normal developmental stages of EC emergence in the embryo (*5*). The EC lineage is one of the earliest to emerge from the primitive streak as mesoderm during gastrulation and has been well studied in model organisms in which differentiation proceeds briskly. Zebrafish ECs are generated from most areas that are composed of mesodermal lineages (*6*). In *Xenopus* animal cap assays, mesoderm retains fate flexibility even after lineage commitment through a controlled balance between Activin and bone morphogenetic protein 4 (BMP4) signaling pathways (*7*). In the chick, some mesoderm-derived ECs are generated within the embryo from committed somites (*8*). Elegant studies using differentiating murine embryonic stem cells (ESCs) have identified specific culture conditions that permit the generation of multiple mesoderm subsets, reflecting embryonic and extraembryonic mesoderm comparability (including the organizing, middle, and posterior primitive streak) (*9*), and ECs have been reported to arise from all of these mesoderm subsets (*10*).

A variety of methods have been used to control the differentiation of hiPSCs into ECs (*11*–*13*). Each of the approaches differentiates the hiPSC through a mesodermal state (*13*, *14*). From a developmental perspective, numerous signaling pathways including vascular endothelial growth factor (VEGF), Notch, Wnt, Hedgehog, transforming growth factor–β (TGF-β), and many transcriptional networks that include Sox factors, E-twenty-six (ETS) factors, β-catenin, Forkhead factors, and Nr2f2 are critical for EC specification from mesoderm (*15*). Using key markers for EC specification from mesoderm (*5*, *16*), we now report on a method to generate ECs displaying properties

---

[1] Department of Pediatrics, Indiana University School of Medicine, Indianapolis, IN 46202, USA. [2] Department of Surgery, Indiana University School of Medicine, Indianapolis, IN 46202, USA. [3] Department of Ophthalmology and Visual Sciences, University of Alabama at Birmingham (UAB), Birmingham, AL 35294, USA. [4] Astellas Institute for Regenerative Medicine (AIRM), Westborough, MA 01581, USA. [5] Medical Scientist Training Program (MSTP), School of Medicine, University of Alabama at Birmingham, Birmingham, AL 35294, USA. [6] Department of Physiology II, Nara Medical University, Kashihara, Nara 634-8521, Japan. [7] Center for Regenerative Medicine, Pulmonary Center, and Department of Medicine, Boston University School of Medicine, Boston, MA 02118, USA. [8] Department of Endodontics, Hamdan Bin Mohammed College of Dental Medicine, Mohammed Bin Rashid University of Medicine and Health Sciences, Dubai 00000, UAE. [9] Department of Medicine, Ansary Stem Cell Institute, Weill Cornell Medicine, New York, NY 10021, USA. [10] Department of Microbiology and Immunology, Indiana University School of Medicine, Indianapolis, IN 46202, USA. [11] Zhongshan-Xuhui Hospital and Shanghai Key Laboratory of Medical Epigenetics, Institutes of Biomedical Sciences, Fudan University, Shanghai 310104, China. [12] Flow Cytometry Core Facility, Memorial Sloan Kettering Cancer Center (MSKCC), New York, NY 10065, USA. [13] Department of Ophthalmology, Casey Eye Institute, Oregon Health and Science University, Portland, OR 97239, USA. [14] Department of Stem Cell Biology, School of Medicine, Konkuk University, Seoul 05029, Republic of Korea. [15] Indiana Center for Regenerative Medicine and Engineering, Indiana University School of Medicine, Indianapolis, IN 46202, USA.

*Corresponding author. Email: mariagrant@uabmc.edu (M.B.G.); myoder@iu.edu (M.C.Y.)

†These authors contributed equally to this work.

similar to umbilical cord blood and adult peripheral blood endothelial colony-forming cells (ECFCs) (*17*) via a specific mesoderm subset displaying features of posterior lateral mesoderm.

ECFCs are primary human ECs that reside in the blood vessels of human individuals, circulate in very low numbers in peripheral blood, and display a hierarchy of clonal proliferative potential and in vivo vessel-forming ability (*18*, *19*). ECFCs have been purported to be a potential source of reparative cells for ischemic disorders in human individuals (*20*, *21*). Unfortunately, access to primary ECFCs is severely limited by location, rarity in circulating blood, reductions in blood concentration with aging, and risk of dysfunction in disorders, such as diabetes (*22*, *23*). We have previously reported that ECFCs can be derived through a complex and lengthy multistep differentiation protocol from hiPSCs (*17*). In this study, we sought to identify the mesoderm precursor of the ECFCs with high proliferative potential (HPP) to provide a more rapid acquisition of ECFCs and avoid the proliferative stress and costs associated with the prolonged expansion previously required (*17*).

RESULTS

Generating mesoderm cells with potential to differentiate into ECFC-like cells with in vitro and in vivo blood vessel–forming capacity

We developed a serum-free defined mesoderm differentiation protocol to obtain distinct day 4 mesoderm fractions and examined their ECFC differentiation potential (Fig. 1A). In preliminary studies, we cultured the fibroblast-derived hiPSC line (DF19-9-11T) on Matrigel-coated plates in mTeSR1 medium for 2 days (days −2 and 0). To induce the earliest multipotent mesodermal progenitors (*16*), we replaced mTeSR1 medium with Stemline II medium supplemented with Activin-A (10 ng/ml), BMP4 (20 ng/ml), VEGF_{165} (10 ng/ml), and fibroblast growth factor-2 (FGF-2) (10 ng/ml) on day 0 of differentiation. The following day, the culture medium was replaced with fresh Stemline II medium supplemented with BMP4 (20 ng/ml), VEGF_{165} (10 ng/ml), and FGF-2 (10 ng/ml) to promote mesodermal cell differentiation. Because kinase insert domain receptor (KDR), neural cell adhesion molecule (CD56), and/or apelin receptor (APLNR) have previously been used to isolate mesoderm subsets containing hematoendothelial or cardiac precursors in mouse and human ESCs (*16*), we examined the differentiated hiPSC for subsets of cells coexpressing these cell surface proteins using flow cytometry. Of interest, on day 4 of culture, APLNR^+ cells were found only in the $\text{KDR}^+\text{CD56}^+$ mesoderm fraction and CD56 and APLNR coexpression was higher on days 3 and 4 of differentiation (fig. S1, A and B). While day 4 differentiated cells expressed KDR, CD56, and APLNR mesodermal markers (KNA^+ cells), the endothelial markers CD31, Neuropilin-1 (NRP-1), and CD144 were not expressed (fig. S1C), suggesting that the KNA^+ mesoderm subset on day 4 of hiPSC differentiation has not yet committed to the endothelial lineage. $\text{KDR}^+\text{CD56}^+\text{APLNR}^+$ (KNA^+), $\text{KDR}^+\text{CD56}^+\text{APLNR}^-$, and $\text{KDR}^+\text{CD56}^-\text{APLNR}^-$ subsets were isolated at day 4 of differentiation and cultured for another 4, 6, or 8 days (total of 8, 10, or 12 days) to examine for the emergence of $\text{NRP-1}^+\text{CD31}^+$ cells that are known to be enriched with ECFCs (Fig. 1B) (*17*). The KNA^+ mesoderm fraction cultured for 12 days, but not $\text{KDR}^+\text{CD56}^+\text{APLNR}^-$ or $\text{KDR}^+\text{CD56}^-\text{APLNR}^-$ cells, gave rise to a significant percentage of $\text{NRP-1}^+\text{CD31}^+$ cells (Fig. 1, C and E; range, 13 to 23%; n = 10) that formed homogeneous cobblestone endothelial monolayer morphology (Fig. 1D) and displayed near-uniform coexpression for CD31 and CD144 endothelial markers (Fig. 1, D and F; n = 10).

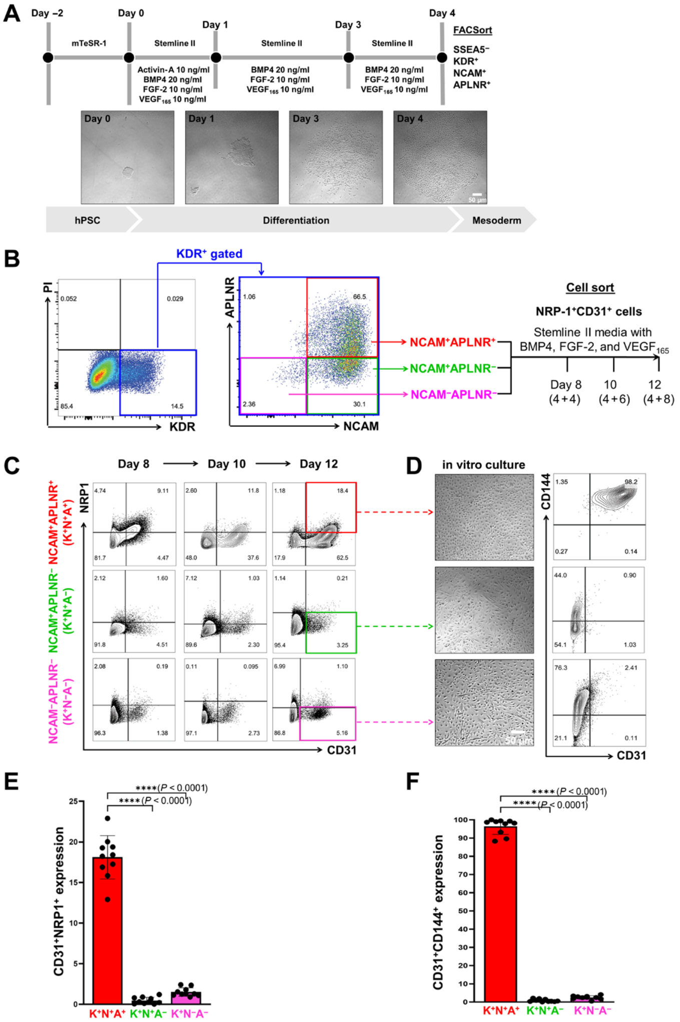

Fig. 1. NCAM and APLNR coexpressing cells within D4 KDR^+ mesoderm cells (KNA^+ mesoderm) give rise to $\text{NRP-1}^+\text{CD31}^+$ ECs with ECFC competence. (**A**) Schematic of simple one-step, two-dimensional, serum and feeder-free mesoderm lineage differentiation protocol. (**B**) Sorting strategy for day 4 (D4) differentiated hiPSCs. KDR^+ cells were gated for NCAM and APLNR expression. $\text{KDR}^+\text{NCAM}^+\text{APLNR}^+$ ($\text{K}^+\text{N}^+\text{A}^+$), $\text{KDR}^+\text{NCAM}^+\text{APLNR}^-$ ($\text{K}^+\text{N}^+\text{A}^-$), and $\text{KDR}^+\text{NCAM}^-\text{APLNR}^-$ ($\text{K}^+\text{N}^-\text{A}^-$) cells were sorted for further differentiation and examination for the emergence of $\text{NRP-1}^+\text{CD31}^+$ ECFCs. PI, propidium iodide. (**C**) Sorted $\text{K}^+\text{N}^+\text{A}^+$, $\text{K}^+\text{N}^+\text{A}^-$, and $\text{K}^+\text{N}^-\text{A}^-$ mesoderm subsets were further differentiated into ECFC lineage for another 8 days (4 plus 8, total of 12 days) to examine for the emergence of $\text{NRP-1}^+\text{CD31}^+$ cells at various days of differentiation. (**D**) At day 12, $\text{K}^+\text{N}^+\text{A}^+$ mesoderm fraction gave rise to $\text{NRP-1}^+\text{CD31}^+$ cells that formed a homogeneous cobblestone endothelial monolayer and displayed uniform coexpression for CD31 and CD144 endothelial markers. (**E**) Sorted $\text{K}^+\text{N}^+\text{A}^+$, $\text{K}^+\text{N}^+\text{A}^-$, and $\text{K}^+\text{N}^-\text{A}^-$ mesoderm subsets were further differentiated into ECFC lineage for 4 + 8 days to examine for the emergence of $\text{CD31}^+\text{NRP-1}^+$ cells at various days of differentiation (n = 10). (**F**) $\text{K}^+\text{N}^+\text{A}^+$ mesoderm fraction gave rise to $\text{CD31}^+\text{NRP-1}^+$ cells and displayed uniform coexpression for CD31 and CD144 endothelial markers (n = 10).

When the KNA^+ cells were differentiated into $\text{NRP-1}^+\text{CD31}^+$ cells (total of 12 days) and were individually deposited into culture wells via cell sorting and examined for EC clonal proliferative potential, the KNA^+-derived cells displayed a complete hierarchy of proliferative potential with a significant proportion (range, 20 to 31%; $n = 10$) of the clones, giving rise to HPP colonies composed of >2001 cells within the 14-day culture period (Fig. 2A). The KDR$^+$CD56$^+$APLNR$^-$ and KDR$^+$CD56$^-$APLNR$^-$ gave rise to few NRP-1$^+$CD31$^+$ cells that, upon cloning, failed to generate significant numbers of HPP colonies of >2001 cells, although less proliferative ECFCs were identified (Fig. 2A). The KNA$^+$-derived NRP-1$^+$CD31$^+$ cells also displayed robust CD144 and lacked alpha–smooth muscle actin (α-SMA) expression (a nonendothelial mesenchymal marker) (Fig. 2B), whereas the NRP-1$^+$CD31$^+$ cells derived from KDR$^+$CD56$^+$APLNR$^-$ and KDR$^+$CD56$^-$APLNR$^-$ cells displayed a mixture of CD144- and α-SMA–expressing cells. Last, KNA$^+$-derived NRP-1$^+$CD31$^+$ cells, but not KDR$^+$CD56$^+$APLNR$^-$ or KDR$^+$CD56$^-$APLNR$^-$ cells, formed robust human blood vessels in vivo (Fig. 2, C and D) when implanted in immunodeficient mice, suggesting a stable cord blood-ECFC–like phenotype (*17*).

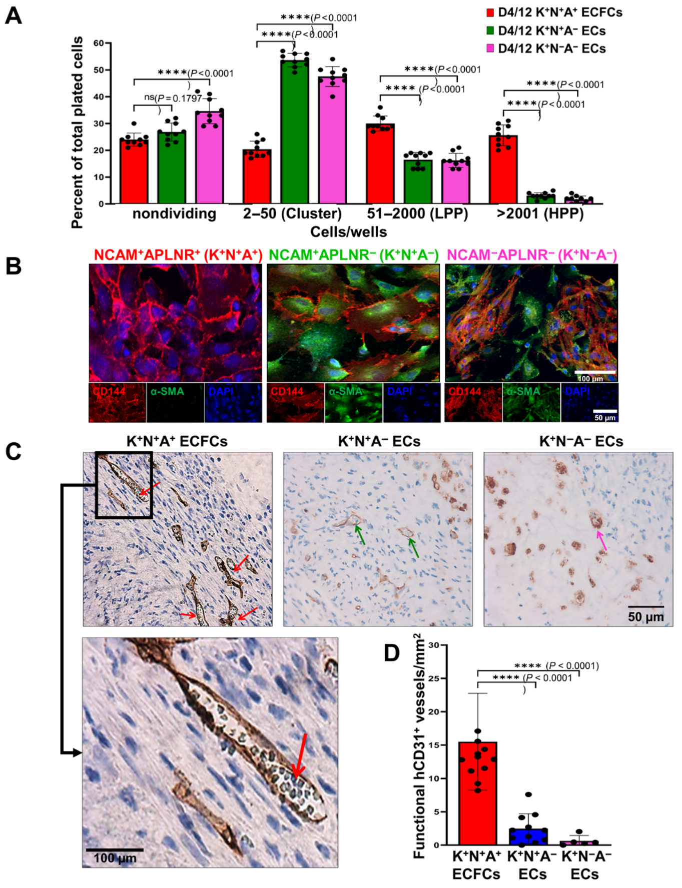

Fig. 2. NRP-1$^+$CD31$^+$ ECs exhibit ECFC competence. (**A**) K$^+$N$^+$A$^+$ mesoderm–derived NRP-1$^+$CD31$^+$ cells exhibited high clonal proliferative potential with a hierarchy of colonies ranging from clusters of 2 to 50 cells up to colonies of >2001 cells similar to that of hiPSC-ECFCs. However, cells isolated from other two subsets failed to exhibit high clonal proliferative potential with marked reduction in colonies of >2001 cells. $n = 10$; means ± SD; *t* test: not significant (ns) and ****$P < 0.0001$. LPP, low proliferative potential. (**B**) At day 12, K$^+$N$^+$A$^+$ mesoderm fraction completely lacked α-SMA expression (top), suggesting a stable ECFC-like phenotype. However, cells isolated from the other two subsets lacked adequate NRP-1 expression, formed heterogeneous cell monolayers, displayed expression for CD144 but lacked uniform coexpression for CD31 and CD144 endothelial markers, and exhibited expression for the nonendothelial marker α-SMA (middle and bottom), suggesting a complete lack of a stable ECFC phenotype (scale bar for the middle panel image). DAPI, 4′,6-diamidino-2-phenylindole. (**C**) K$^+$N$^+$A$^+$ mesoderm–derived NRP-1$^+$CD31$^+$ cells produced robust in vivo human blood vessels, as confirmed by anti-human specific CD31 antibody reactivity, which are filled with host murine red blood cells (indicated by red arrows). K$^+$N$^+$A$^-$ mesoderm–derived NRP-1$^+$CD31$^+$ cells produced modest in vivo human blood vessels, as confirmed by anti-human specific CD31 antibody reactivity, that are filled with host murine red blood cells (indicated by green arrows). K$^+$N$^-$A$^-$ mesoderm–derived NRP-1$^+$CD31$^+$ cells produced rare in vivo human blood vessels, as confirmed by anti-human specific CD31 antibody reactivity, that are filled with host murine red blood cells (indicated by pink arrows). (**D**) Quantification of functional hCD31$^+$ blood vessels displaying equivalent formation of vessels between hiPSC-ECFCs and K$^+$N$^+$A$^+$ ECFCs and significantly reduced in K$^+$N$^+$A$^-$ ECs or K$^+$N$^-$A$^-$ ECs. $n = 13$ (K$^+$N$^+$A$^+$ ECFCs), $n = 11$ (K$^+$N$^+$A$^-$ ECs), and $n = 5$ (K$^+$N$^-$A$^-$ ECs); means ± SD; *t* test: ****$P < 0.0001$.

Recently, an antibody against Stage-Specific Embryonic Antigen-5 (SSEA-5) glycan on hiPSCs was used to eliminate pluripotent teratoma-forming cells from hiPSC differentiation protocols (*24*). We confirmed that the SSEA-5 antibody could be successfully used to deplete undifferentiated or partially differentiated hiPSC (SSEA-5$^+$KNA$^-$) that formed teratomas from our nonteratoma-forming day 4 SSEA-5$^-$KNA$^+$ mesoderm cells (Fig. 3A and figs. S2, A and B, and S3). Our hiPSC-derived SSEA-5$^-$KNA$^+$ mesoderm cells expressed markers for posterior lateral plate mesoderm and lacked expression for markers associated with axial, paraxial, and intermediate mesoderm subsets (Fig. 3B and table S1). Direct in vivo implantation of this mesoderm subset formed robust vessels expressing NRP-1$^+$CD31$^+$ cells (Fig. 3, C and F). We confirmed the stemness of SSEA-5$^+$KNA$^-$ teratoma-forming cells at day 4 (fig. S2B). In vivo implantation of SSEA-5$^-$KNA$^+$ and SSEA-5$^-$KNA$^-$ mesoderm cells was performed to examine their potential for direct in vivo differentiation into blood vessels that are similar to ECFC-derived vessels (Fig. 3, D to F). While SSEA-5$^-$KNA$^+$ cells formed robust functional in vivo vessels (red arrows, left), SSEA-5$^-$KNA$^-$ cells failed to form robust in vivo vessels (blue arrows, right) as shown by the quantification of functional hCD31$^+$ blood vessels (Fig. 3, D and E) ($P < 0.0002$). SSEA-5$^-$KNA$^+$ cells formed NRP-1$^+$CD31$^+$ ECFC vessels as early as 8 days after implantation (Fig. 3F).

Nondiabetic KNA$^+$ cells and diabetic KNA$^+$ cells exhibit similar phenotypic characteristics, in vitro function, and transcriptomic expression profiles

We next examined the differentiation characteristics of KNA$^+$ cells from healthy controls. We observed the experimental timeline and differentiation of KNA$^+$ from nondiabetic controls (N-KNA; $n = 4$) during a 4-day time course (fig. S4). We subsequently examined the differentiation characteristics of KNA$^+$ cells from diabetic donors (D-KNA$^+$; $n = 3$) and found them to be similar (fig. S4). The clinical characteristics of control and diabetic donors used to generate the hiPSC lines are described in table S2.

The diabetic retina represents an environment rich in hypoxia-regulated factors that facilitate the migration of reparative cells toward areas of injury. For KNA$^+$ cells to migrate from the vitreous into the retina, they need to express receptors for the growth factors expressed by the injured retina, such as C-X-C Motif Chemokine Ligand 12 (CXCL12) and insulin-like growth factor 1 (IGF-1). KNA$^+$ cells were established from N-KNA$^+$ and D-KNA$^+$ donors. The percentage of N-KNA$^+$ and D-KNA$^+$ cells expressing CXCR4 (receptor of CXCL12), IGF1R, and CD146 (marker for endothelial linage) was quantified (fig. S4). On average, approximately 50% of N-KNA$^+$ and D-KNA$^+$ cells express CXCR4, while nearly all hiPSC-KNA$^+$ cells express IGF1R and CD146 (~88%).

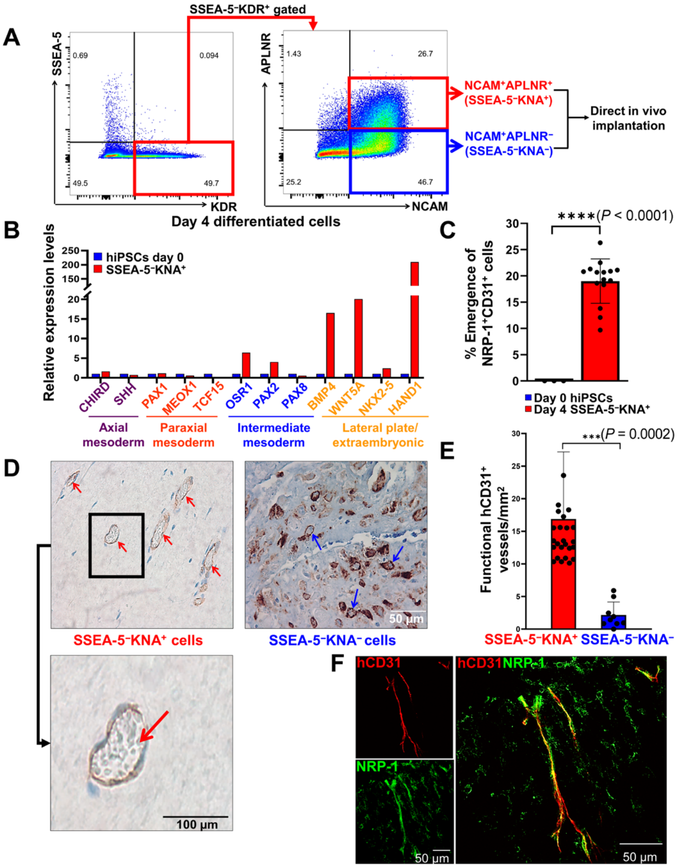

Fig. 3. Cell sorting strategy for D4 SSEA-5–depleted KNA$^+$ mesoderm cells and direct in vivo differentiation of S$^-$KNA$^+$ mesoderm cells that formed robust human blood vessels without giving rise to teratomas. (**A**) Cell sorting strategy for D4 differentiated hiPSCs–derived mesoderm cells. SSEA-5$^-$KDR$^+$ cells were gated for NCAM and APLNR expression. SSEA-5$^-$KDR$^+$NCAM$^+$APLNR$^+$ (SSEA-5$^-$KNA$^+$) and SSEA-5$^-$KDR$^+$NCAM$^+$APLNR$^-$ (SSEA-5$^-$KNA$^-$) cells were sorted for further analysis. SSEA-5$^-$KDR$^+$ and SSEA-5$^+$KDR$^-$ cells were sorted for in vivo implantation to examine for teratoma formation and functional vessel formation in the same recipient animal (n = 10). (**B**) D4 SSEA-5–depleted KNA$^+$ mesoderm cells display transcripts typically enriched in lateral plate/extraembryonic mesoderm but lacking expression of axial, paraxial, and intermediate mesoderm markers in SSEA-5$^-$KNA$^+$ cells (n = 3). (**C**) Sorted SSEA-5$^-$KNA$^+$ cells were further differentiated into ECFC lineage for another 8 days (4 plus 8, total of 12 days). At day 12, SSEA-5$^-$KNA$^+$ cells produced ≥3-fold more NRP-1$^+$CD31$^+$ cells compared to NRP-1$^+$CD31$^+$ cells produced after continuous 12 days of differentiation of day 0 hiPSCs (without isolating mesoderm subset at D4 of differentiation) into ECFC lineage. n = 15; means ± SD; t test: ****P < 0.0001. (**D**) D4 SSEA-5$^-$KNA$^+$ mesoderm–derived ECFC vessels remain stable in vivo with completely inosculating with the host vasculature to become part of the host circulation and do not regress to form teratoma after long-term in vivo implantation (≥8 months after implantation). While SSEA-5$^-$KNA$^+$ cells formed robust functional in vivo vessels (red arrows, left), SSEA-5$^-$KNA$^-$ cells failed to form robust in vivo vessels (blue arrows, right). (**E**) Quantification of functional hCD31$^+$ blood vessels (n = 26, SSEA-5$^-$KNA$^+$ and n = 9, SSEA-5$^-$KNA$^-$; means ± SD; t test: ***P = 0.0002. (**F**) Direct in vivo differentiation of SSEA-5$^-$KNA$^+$ cells formed CD31$^+$NRP-1$^+$ blood vessels as early as 8 days after implantation (red, hCD31; green, NRP-1).

In vitro tube formation assay (Fig. 4A) showed that KNA$^+$ cells from both donor types formed capillary networks with similar time frame, tube length (Fig. 4B), and branch points (Fig. 4C). We next differentiated KNA$^+$ cells into ECFCs. ECFCs derived from N-KNA$^+$ cells were similar to ECFCs of diabetic origin (D-ECFCs) when examined for expression of endothelial surface markers. N-ECFCs exhibited the following average percent of expression: CD31 (~70%), CD144 (~98%), NRP-1 (~94%), CD146 (~95%), and KDR (~85%) with similar levels in D-ECFCs (Fig. 4D). Figure 4E shows representative images of tube-forming assay using N-ECFCs and D-ECFCs and displays no significant difference in the morphology of the tubes generated from either the N-ECFCs or the D-ECFCs. Quantification of capillary tube length and number of branch points were also similar (Fig. 4, F and G).

These studies suggest that, in vitro, the diabetic- and nondiabetic-derived KNA$^+$ cells share key molecular pathways regardless of the donor status of the cells used for hiPSC generation. To better understand the transcriptomic landscape of N-KNA$^+$ and D-KNA$^+$ cells, we performed bulk RNA sequencing (RNA-seq) on N-KNA$^+$, D-KNA$^+$, and the hiPSCs from which they were derived. As expected, N-KNA$^+$ and D-KNA$^+$ cells expressed uniquely high levels of mesoderm- and EC-specific markers including KDR, APLNR, Neural Cell Adhesion Molecule 1 (NCAM1), and Guanine-adenine-thymine-adenine 2 (GATA2) (Fig. 5A). Conversely, N-hiPSCs and D-hiPSCs expressed high levels of embryonic stem markers including SRY (sex determining region Y)–box 2 (SOX2), Octamer-binding transcription factor 4 (OCT4), Homeobox protein NANOG (NANOG), and Krupper-like factor 4 (KLF4) (Fig. 5A). Linear regression comparing the gene expression profiles of N-hiPSCs and D-hiPSCs demonstrated that these cells showed greater transcriptomic differences [R^2 = 0.89, 130 differentially expressed genes (DEGs); Fig. 5B] than that of the N-KNA$^+$ and D-KNA$^+$ cells derived from these cells (R^2 = 0.96, 29 DEGs; Fig. 5C). Spearman correlation confirmed that N-KNA$^+$ and D-KNA$^+$ cells were indeed more similar than their N-hiPSC and D-hiPSC counterparts (Fig. 5D). These findings suggest that KNA differentiation of N-hiPSCs and D-hiPSCs is sufficient to modulate the baseline gene expression differences caused by diabetic status in reprogrammed somatic cells to a pattern similar to KNA derived from N-hiPSCs.

Incorporation of KNA$^+$ cells into retinal vessels of *db/db* mice and nonhuman primates

In these studies, we used the retinal microvaculature as a representative vascular bed that is well known to be dysfunctional in diabetes, as it is critical to the therapeutic rigor of a cell population to test it in a diseased environment. At 1 month after intravitreal injection, N-KNA$^+$ cells (Fig. 6, A, C, and E, and movies S1 and S2) and, to a slightly lesser extent, D-KNA$^+$ cells (Fig. 6, B and D) were observed to be incorporated into the damaged retinal vessels of *db/db* mice. In contrast, both cell types displayed a random distribution around the uninjured retinal vessels of control *db/m* mice (fig. S5, A and B). Human KNA$^+$ cells, detected by using anti-human–specific CD31 antibody, were found intercalated into the mouse vasculature as detected by anti-mouse CD31 antibody labeling (Fig. 6, A to E). In the retina of *db/db* mice, N-KNA$^+$ cells were found connecting with the retinal vessels of the superficial, intermediate, and deep plexus. Confirmation that the hiPSCs incorporated into murine vasculature was achieved by collagen IV staining of the murine vascular basement membrane and identification of the human cells with human nuclear antigen (fig. S5). To assess whether KNA$^+$ cells could be considered as a viable strategy for use in clinical trials, we labeled cells with green fluorescent protein (GFP) to facilitate their visualization and then injected them into a healthy nonhuman primate (NHP). N-KNA$^+$ cells were found in the superficial vascular plexus (Fig. 7, A to C) at

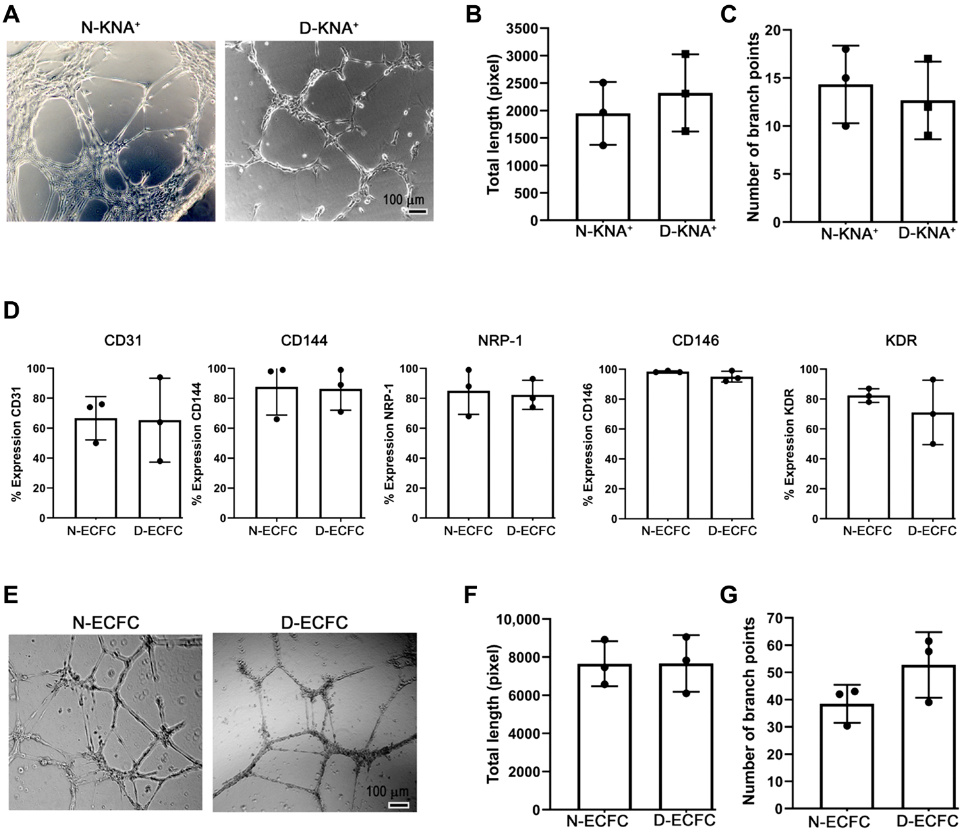

Fig. 4. In vitro tube formation and quantification of endothelial surface marker from ECFC. (**A**) Representative images of the characteristic capillary networks generated by KNA$^+$ cells on Matrigel. (**B** and **C**) Quantification of tube formation assay with bar diagram of total vessel length (B) and branch points (C). (**D**) Expression pattern of different endothelial markers in KNA$^+$ cells derived from ECFCs of either nondiabetic (N-ECFC) or diabetic (D-ECFC) origin. N-ECFC and D-ECFC cells were stained with antibodies for CD31, CD144, NRP-1, CD146, and KDR. After flow cytometry analysis, the percentage of cells expressing each cell surface marker is presented in the bar graph. (**E**) Analysis of the tube formation assay using N-ECFCs and D-ECFCs. Representative images of characteristic capillary networks on Matrigel. (**F** and **G**) Bar graph of total length (F) and branching point analysis are presented (G).

2 weeks after injection, suggesting that GFP$^+$ N-KNA$^+$ cells can migrate through the vitreous and reach the retina of NHP.

We next used flow cytometry on dissociated neural retinas from cell-injected versus saline-injected eyes in 6-month-old *db/db* mice to confirm revascularization. One month after injection, N-KNA$^+$– and D-KNA$^+$–injected eyes showed an increased proportion of CD31$^+$ CD144$^+$ ECs compared to saline-injected contralateral controls (Fig. 7D). Together, the cell-injected eyes showed a significant four times increase in CD31$^+$ CD144$^+$ ECs compared to saline-injected controls (Fig. 7E).

In vivo retinal imaging revealed no retinal toxicity following KNA$^+$ cell injection

For this part of the study, we used two strains of *db/db* mice, B6.BKS(D)-*Lepr*^{db}/J and BKS.Cg-*Dock7*^{m} +/+ *Lepr*^{db}/J. These two strains exhibit different degrees of diabetes and were used to more accurately reflect the marked variation of glucose control seen in diabetic subjects and to discern whether the severity of diabetes in the host affects the function of the KNA$^+$ cells. B6.BKS(D)-*Lepr*^{db}/J mice have less severe diabetes, with most mice demonstrating blood glucoses between 250 and 350 mg/dl from weeks 4 to 20 of diabetes and with a typical life span of 18 to 20 months. In contrast, the BKS.Cg-*Dock7*^{m} +/+ *Lepr*^{db}/J strain develops a more severe hyperglycemia (on average, >350 mg/dl), with a life span of typically less than 12 months.

B6.BKS(D)-*Lepr*^{db}/J mice were first examined at 1 month after injection (fig. S6, A and B). No retinal pathology was observed by fundus imaging, and total retinal thickness as well as thickness of the retinal nerve fiber layer and the inner plexiform layer were identical in eyes injected with cells or saline (fig. S6, C and D). No vascular pathology could be detected on fluorescence angiography at 1 month after injection (fig. S6E). At 3 months after injection, OCT showed normal-appearing retina in *db/db* mice injected with N-KNA$^+$ cells or saline (fig. S7A), and no fluorescein leakage or vascular abnormalities were detected in N-KNA$^+$ cell– or saline-injected eyes (fig. S7B). Similar findings were obtained in BKS.Cg-*Dock7*^{m} +/+ *Lepr*^{db}/J cohorts injected with KNA$^+$ cells (fig. S8, A and B).

Intravitreal injection of KNA$^+$ cells rescues visual function in *db/db* eyes

Electroretinograms (ERGs) measure the electrical response of the retina to light stimuli and demonstrate the function of multiple retinal cell types by the analysis of individual waveform components. We performed intravitreal injections of KNA$^+$ cells in the eyes of

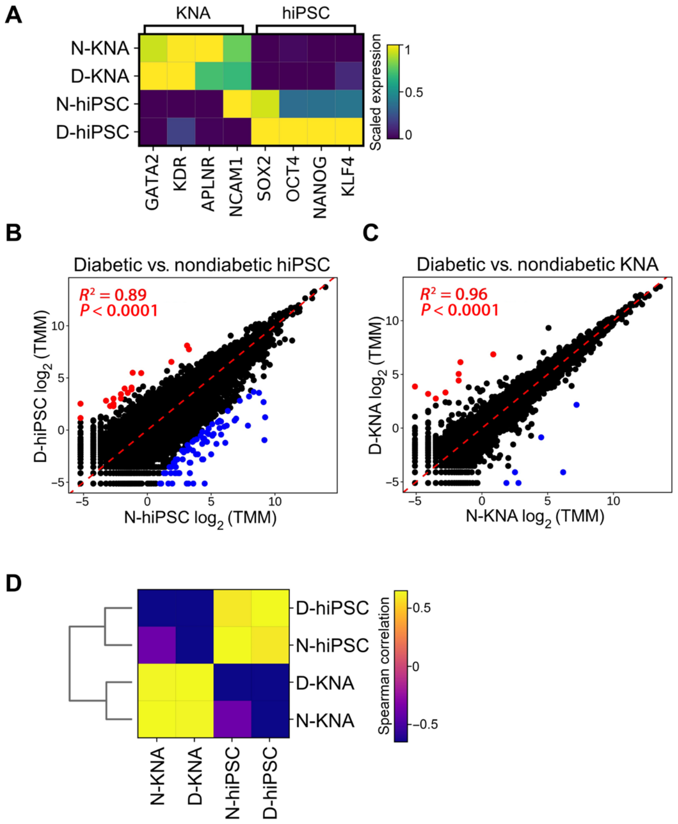

Fig. 5. Transcriptomic analysis demonstrates that KNA cells from nondiabetic and diabetic donors are highly similar. (**A**) Expression of KNA and hiPSC marker genes. (**B** and **C**) Bulk RNA-seq comparison of diabetic-derived hiPSCs (D-hiPSC) versus nondiabetic-derived hiPSCs (N-hiPSC) (B) and diabetic-derived KNA cells (D-KNA) versus nondiabetic-derived KNA cells (N-KNA) (C). Red dots were significantly up-regulated genes and blue dots were significantly down-regulated genes in diabetic-derived cells. TMM, trimmed mean of *M* values. (**D**) Spearman correlation of all four samples using three principal components.

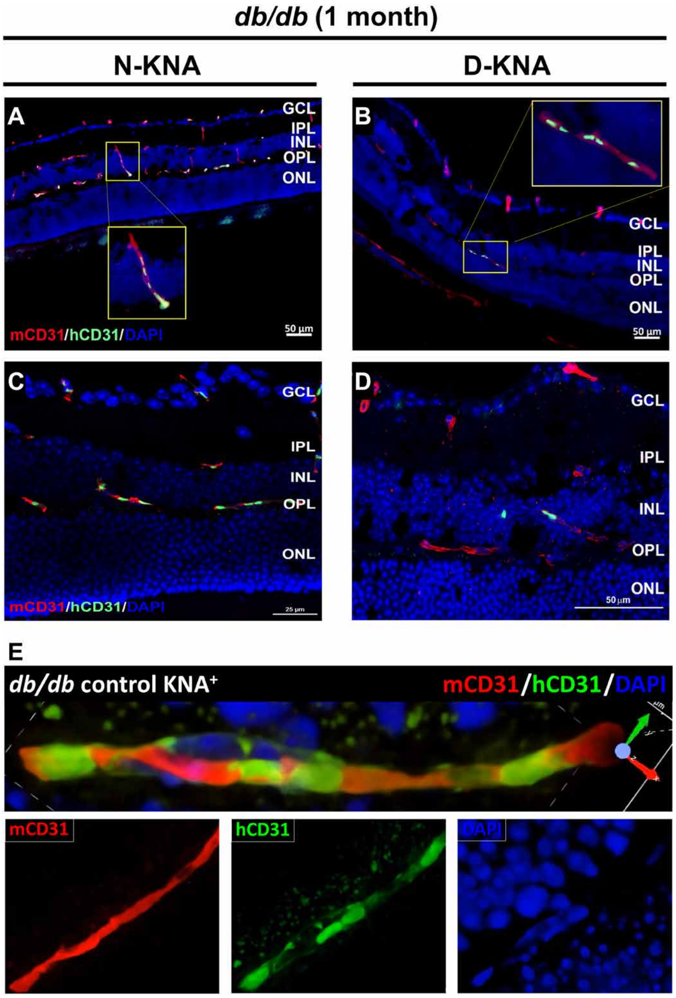

Fig. 6. KNA$^+$ cells from nondiabetic and diabetic donors integrate into retinal blood vessels of *db/db* mice 1 month after injection. (**A** to **E**) Representative immunofluorescence images of retinal frozen sections stained with anti–human CD31 (hCD31) (green) and anti–mouse CD31 (mCD31) (red) antibodies. Viable human nondiabetic (N-KNA$^+$) (A, C, and E) and diabetic (D-KNA$^+$) (B and D) cells were detected in the *db/db* mouse retinas and incorporated into the small vessels of the vascular plexus. Nuclei were stained with DAPI (blue). Insets in (A) and (B) show cell incorporation at higher magnification. IPL, inner plexiform layer; GCL, ganglion cell layer; INL, inner nuclear layer; OPL, outer plexiform layer; ONL, outer nuclear layer.

6-month-old diabetic BKS.Cg-*Dock7^m* +/+ *Lepr^{db}*/J mice. Representative ERG waveforms with quantification of maximum amplitudes from 1 month after injection with N-KNA$^+$ or D-KNA$^+$ cells are displayed (fig. S9A). The scotopic b-wave amplitude was significantly increased in *db/db* mice injected with N-KNA$^+$ cells compared to *db/db* mice injected with saline (fig. S9B). We observed a trend toward improvement of scotopic a-wave in the *db/db* eyes with D-KNA$^+$ cells compared to saline-injected *db/db* eyes ($P = 0.0512$). A significant improvement in visual acuity 1 month after injection was observed in BKS.Cg-*Dock7^m* +/+ *Lepr^{db}*/J mice injected with either N-KNA$^+$ cells or D-KNA$^+$ cells compared to saline-injected eyes (fig. S9C).

Proteomic studies demonstrate multimodal retinal signaling pathways influenced by KNA$^+$ cells

To better understand the potential molecular mechanisms underlying the beneficial effects of N-KNA$^+$ and D-KNA$^+$ cell administration, we performed proteomic studies on retinal homogenates (Fig. 7, F and G). Retinas of *db/db* mice were intravitreally injected with either saline, N-KNA$^+$, or D-KNA$^+$ and were harvested 1 month after injection. Compared to saline-injected eyes, the proteomic analysis of retinal homogenates from mice injected with N-KNA$^+$ cells, and to a lesser degree, D-KNA$^+$ cells, showed a marked reduction in hypoxia-inducible factor 1α (HIF1α) and VEGF receptor 2 (VEGFR2) expression. Retinal homogenates from mice injected with D-KNA$^+$ cells, and to a lesser degree, N-KNA$^+$ cells, showed a marked decrease in expression of hexokinase (HK) and mammalian target of rapamycin (mTOR) compared to saline-injected eyes. Administration of N-KNA$^+$ cells resulted in increased expression of FGF-2 (vascular and neuroprotective) (*25*), STAT3 (signal transducer and activator of transcription 3) (cellular repair) (*26*), Vav Guanine Nucleotide Exchange Factor 1 (VAV1) [formation of endothelial tight junctions by increasing Yes-associated protein 1 (YAP)] (*27*), Mnk1 [activated in response to extracellular signal–regulated kinase 1 and p38 Mitogen-activated protein (MAP) kinases] (*28*), and Cytochrome c oxidase IV (COX IV) [energy homeostasis and adenosine triphosphate (ATP) generation] (*29*). D-KNA cell injection resulted

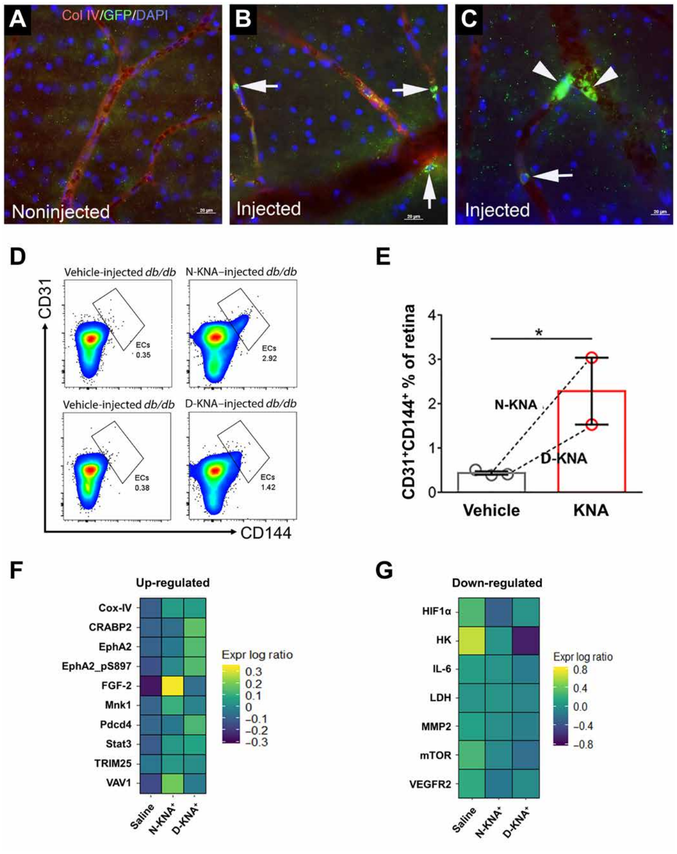

Fig. 7. Retinal flow cytometry confirms revascularization following injection of either nondiabetic or diabetic KNA cells in *db/db* mice and flat-mount macaque retinas triple-stained with Collagen IV (Col IV) (red), GFP (green), and DAPI (blue). (**A**) Images from noninjected retinas. (**B** and **C**) Images from retinas 2 weeks after intravitreous injection of GFP^+ nondiabetic KNA^+ cells. Arrows in (B) and (C) point to GFP^+/KNA^+ cells. Arrowheads in (C) indicate GFP^+/KNA^+ cells becoming part of blood vessels. Scale bars, 20 μm (A to C). (**D**) Whole retina flow cytometry of paired contralateral *db/db* eyes injected with vehicle and either nondiabetic (N-KNA) or diabetic (D-KNA) KNA cells. (**E**) Quantification of $CD31^+CD144^+$ (VE-cadherin) ECs from whole retina flow cytometry. Student's *t* test; $^*P < 0.05$. (**F** and **G**) Heatmap of differentially expressed proteins between all treatment groups. KNA^+ cell administration reestablishes physiologic levels of these factors, potentially promoting retinal neural protection, improving retinal metabolism, decreased inflammation, and reduced angiogenic activity. Proteomic analysis indicating either up-regulation or down-regulation, relative to saline, of retinal proteins from *db/db* mice injected with either nondiabetic ($N\text{-}KNA^+$) or diabetic ($D\text{-}KNA^+$) KNA cells. IL-6, interleukin-6.

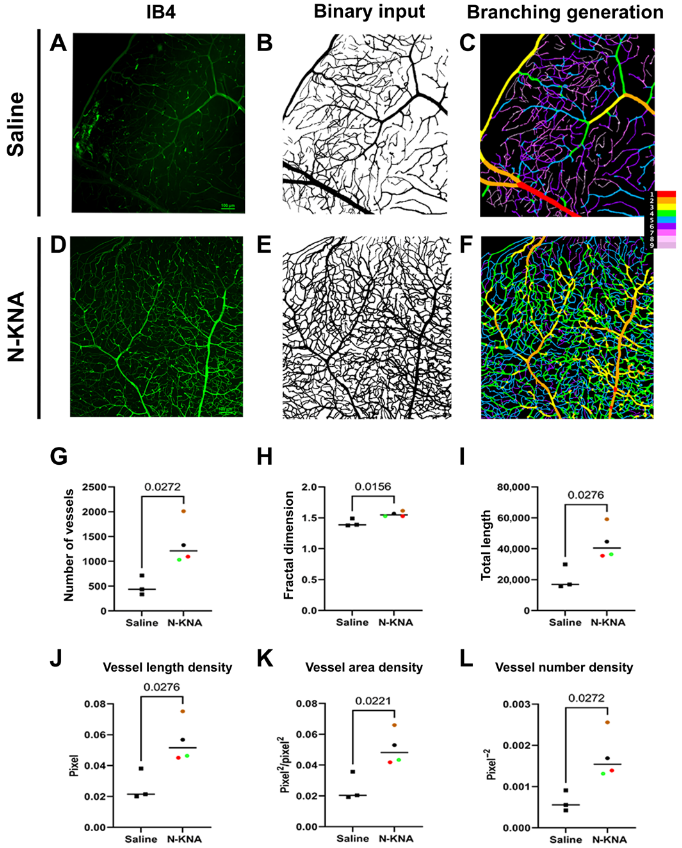

Fig. 8. Vascular density assessment in retinas of *db/db* mice injected with either saline or N-KNA cells. (**A** and **D**) Saline (A) and N-KNA cells (D). Retinal flat mount from *db/db* cohorts stained with Griffonia Simplicifolia Lectin I IB4 (green), revealing a significant improved perfusion in treated eye. (**B** and **E**) Binary input image of saline- and N-KNA–treated perfused retinal flat mounts. (**C** and **F**) Branching generation detected by VESGEN software identifies each generation (1 to 9) with a specific color code from largest to smallest branches. (**G** to **L**) Graphs show VESGEN quantification data. Changes in the number of vessels (G), fractal dimension (characterizes the structural changes from large vessels to small vessels across the retina) (H), total length (the summation of the length of all vessels in the ROI) (I), vessel length density (total length/ROI) (J), vessel area density (vessel area/ROI) (K), and vessel number density (vessel number/ROI) (L). All parameters indicate a restoration of retinal vascularity with N-KNA cell treatment compared to saline control injection.

in increased expression of Cellular Retinoic Acid Binding Protein 2 (CRABP2) (retinoid metabolism and the visual cycle) (*30*), EphA2 (neurogenesis and monocyte-endothelial interactions) (*31*), and programmed cell death (Pdcd) (epithelial cell polarity) (*32*, *33*).

Vascular density assessment in retinas of *db/db* mice injected with either saline or N-KNA cells

Last, we demonstrate the effect of N-KNA cell administration on retinal vascular perfusion. For this assessment, we used a series of nine parameters using VESsel GENeration (VESGEN) Analysis software (*34*–*37*). VESGEN uses a binary vascular image and automated output that provides informative vascular maps with quantification of key vascular parameters (Fig. 8, A to F). Using VESGEN, we observed that the number of vessels within a standardized region of interest (ROI) was increased in the retinas of mice injected with N-KNA cells compared to those injected with saline (Fig. 8G). Fractal dimension was calculated as an index of vascular complexity, typically characterized as the space-filling capacity of a vascular pattern, and demonstrated an increase in the retinas of the N-KNA cell–injected *db/db* mouse eyes compared with saline (Fig. 8H). Additional parameters of vascularity included the following: vessel length (total of all vessels in ROI; Fig. 8I); vessel length density, which represents the vessel length/ROI (Fig. 8J); vessel area density, which is the vessel area/ROI (the amount of area taken up by the vessels within the ROI; Fig. 8K); and vessel number density, which is the vessel number/ROI (Fig. 8L). All vascular parameters indicated restoration of retinal vascularity in N-KNA–treated retinas compared to saline-treated diabetic retinas.

DISCUSSION

In this study, we demonstrate the use of a unique hiPSC-derived mesodermal population that promotes robust microvascular repair without any evidence of toxicity. This population was characterized on the basis of expression of VEGFR2, NCAM, and APLNR (KNA$^+$ cells). Both nondiabetic and diabetic donors were used to generate hiPSC lines, and in vitro and in vivo studies were performed to interrogate their function. KNA$^+$ cells from nondiabetic and diabetic sources expressed similar chemokine receptors, formed equivalent numbers of tubes and branching points in a two-dimensional (2D) angiogenic assay, and expressed a near-identical transcriptome. Intravitreally injected N-KNA$^+$ and D-KNA$^+$ cells migrated to the retinal surface, homed to sites of vascular damage, incorporate into resident vasculature, and remained viable. Using in vivo retinal imaging, no evidence of retinal toxicity was observed and the injection of N-KNA$^+$ or D-KNA$^+$ cells was able to not only correct vascular abnormalities but also improve retinal function as assessed by ERGs and improve visual acuity as assessed by optokinetic nystagmus (OKN) in *db/db* mice.

ECs have been reported to arise from axial, paraxial, lateral, intermediate, and posterior mesoderm subsets (*9*, *10*). A variety of methods have been used to control the differentiation of hiPSCs into ECs [reviewed in (*13*)]. In general, hiPSCs are differentiated into ECs via three approaches: differentiation in coculture with stromal cells, formation of 3D embryoid bodies, or 2D feeder-free monolayer cultures (the most common method) (*13*). Manipulating the signaling pathways that specify mesoderm differentiation from the hiPSC is common to the monolayer differentiation systems as used in the present study. Thus, growth factors such as Activin-A, BMP4, and basic FGF are commonly used (*13*, *16*, *17*). GSK-3 (glycogen synthase kinase 3) inhibitors such as CHIR99021 and BIO (6-bromoindirubin-3′-oxime) are also frequently added to promote canonical Wnt signaling pathway, which stimulates the differentiation of the hiPSC-derived mesoderm toward the endothelial lineage (*14*). VEGF is the most common growth factor that is used during this phase (*13*, *16*). Inhibition of the TGF-β signaling pathway has been reported to be crucial for promoting the endothelial specification from mesoderm cells and to avoid endothelial-to-mesenchymal transition in some protocols (*14*). We now report on a method to generate ECFCs, displaying properties similar to umbilical cord blood and adult peripheral blood ECFCs (*17*), via a specific mesoderm subset displaying features of posterior/lateral mesoderm. This is a novel observation as only a single group has reported that ECFCs similar to umbilical cord blood–derived cells can be derived through a multistep differentiation protocol with VEGF$_{165}$ signaling through NRP-1 and VEGFR2 (*17*). The present protocol builds upon that foundation to identify and define the mesoderm precursor of the ECFC. Whether other published hiPSC-derived endothelial differentiation protocols produce ECFCs awaits determination through application of single-cell colony-forming assay analytics using those protocols, but several approaches (coculture with stromal cells or 3D embryoid body formation) have been reported to lack EC derivation with high proliferative ECFC properties (*17*).

Depletion of SSEA-5 glycan on hiPSCs eliminates potential teratoma-forming cells from hiPSC differentiation protocols (*24*). The SSEA-5$^-$KNA$^+$ cells when injected in vivo integrated into the retinal vasculature of diabetic mice, and those treated animals displayed greater retinal vascular perfusion than saline-treated controls. No evidence of injury to the retina was demonstrated by multiple modalities, and visual acuity was improved in the diabetic animals receiving S$^-$KNA$^+$ cells. Thus, the beneficial effects of the KNA$^+$ cells on retinal function (OKN and ERG) are believed to be due to the direct incorporation and differentiation of cells into ECs, restoring the patency of degenerated retinal vessels (with improved perfusion as supported by studies using VESGEN to analyze patent/perfused vasculature) and also by the release of tropic factors (supported by signaling array studies). Neural electrophysiological dysfunction occurs early before vascular abnormalities in diabetic retinopathy (*38*). As we described herein, KNA$^+$ cells restored neuronal function in the retina of *db/db* mice and prevented the earliest changes in diabetic retinopathy progression (*39*).

Proteomic analysis of retinal homogenates from mice injected with KNA$^+$ cells showed reduction in key pathological signaling pathways. HIF1α and VEGFR2 were reduced by the administration of N-KNA$^+$ cells and also reduced, but less so, by the administration of D-KNA$^+$ cells. HIF1α signaling enhances glycolysis by increasing the expression of GLUT1 (Glucose transporter 1) and HK II (Hexokinase II) (*40*), and, as would be expected with reductions of HIF1α, a concomitant decrease in HK II expression was observed. Proteomic analysis of retinal homogenates also showed a decrease in expression of lactate dehydrogenase following D-KNA$^+$ cell injection, more so than N-KNA$^+$ cells, suggesting that the diabetic cells may be more metabolically robust than the nondiabetic cells because of preconditioning in the diabetic environment. Furthermore, when compared with both saline- and N-KNA$^+$ cell–injected retinas, the retinas of mice injected with D-KNA$^+$ cells showed the greatest decrease in expression of matrix metalloproteinase 2 (MMP2), a type IV collagenase that has been shown to play an essential role in retinal angiogenesis. The decrease in MMP2 expression in the retina of the mice injected with KNA$^+$ cells corroborates our previous findings regarding the role of MMP2 in diabetic retinopathy (*41*). In the retinas of mice injected with D-KNA$^+$ cells compared to saline- and N-KNA$^+$ cell–injected retinas, we observed a greater reduction of interleukin-6, a cytokine known to mediate inflammatory damage in the retina, and of mTOR. mTOR functions as a serine/threonine protein kinase that regulates cell growth, cell proliferation, cell motility, cell survival, protein synthesis, autophagy, and transcription (*42*).

We found several proteins increased in response to N-KNA$^+$ cell administration. VAV1, classically known for its role in hematopoiesis, is a guanine nucleotide exchange factor for the Rho family of guanosine triphosphate binding proteins that activate pathways important for cell migration (*43*). Vav1 modulates responses to protein tyrosine kinases. We observed a marked increase in FGF-2 expression in the N-KNA–treated retinas (*44*). The vascular protective effects of VEGF are highly amplified by FGF-2 (*45*). FGF-2 also provides neurotrophic effects protecting against photoreceptor damage and retinal degeneration and, in the context of our study, may be responsible in part for the improvement that we observed in the ERG and OKN of KNA$^+$ cell–treated eyes (*46*). We observed an increase in STAT3 and phospho-STAT3 following N-KNA cell treatment. STAT3 associates with the pyruvate dehydrogenase complex E1 and accelerates the conversion of pyruvate to acetyl coenzyme A, elevates the mitochondrial membrane potential, and promotes ATP synthesis (*47*). Phospho-STAT3 participates in reparative processes (*47*) and may explain, in part, the beneficial retinal effects observed. Mnk1 plays important roles in controlling signals involved in mRNA translation (*48*) and is activated in response to treatment with growth factors and mitogens (*28*). Last, we observed an increase in cytochrome c oxidase subunit 4 isoform 1 (*49*), the oxygen-accepting and rate-limiting step of the respiratory chain that regulates the supply of variable ATP demands in cells, supporting that KNA$^+$ cell treatment could be improving retinal metabolism.

In the D-KNA–treated retinas, we observed an increase in EphA2 that interacts with and phosphorylates YAP protein, leading to its stabilization, nuclear translocation, and activation (*50*). YAP plays a key role in retinal barrier characteristics (*51*), so it is plausible that D-KNA administration by the activation of EphA2 may have contributed to the restoration of retinal barrier integrity in the leaky retinas of diabetic mice. EphA2 can also preserve neuronal function during ischemic stress (*52*) and thus may have served to maintain neuronal function in the microvasculature. Tripartite motif-containing protein 25 (TRIM25) was increased and maintains endoplasmic reticulum homeostasis under adverse conditions, and its up-regulation ameliorates oxidative stress. TRIM25 directly targets Keap1 by ubiquitination and degradation, leading to Nrf2 activation, which bolsters antioxidant defense and cell survival (*53*). NRF 2 is reduced in diabetic retinopathy and thus the exogenous administration of KNA cells may, in part, benefit the retina by activation of this protective pathway (*54*). We also observed an increase in Pdcd4, an inhibitor of protein translation (*33*). Preservation of Pdcd4 is important for expression of epithelial barrier proteins including maintenance of epithelial polarity (*33*), which, in the retina, could potentially be critical for retinal pigment epithelial cell function that is compromised in the retina of diabetic mice. In the D-KNA cell–treated mice, we also observed an increase in CRABP2, known for its ability to regulate retinoic acid (RA) binding to nuclear RA receptors. Retinoid CRABP2 serves to protect RA, a scarce resource, from dispersing into cell membranes and/or undergoing catabolism (*55*). Thus, proteomic studies suggest that KNA$^+$ cell administration results in activation of key protective pathways in the retina and inhibition of deleterious pathways.

Our study has some limitations including that we did not investigate whether administration of D-KNA$^+$ cells would increase the number of perfused retinal vessels as we showed for N-KNA (Fig. 8). We are unable to make a direct quantitative comparison of D-KNA$^+$ cell function to N-KNA$^+$ cell function without performing additional studies using a larger sampling of patient-derived hiPSC lines. Live blood flow studies, while technically difficult in rodents, would provide evidence beyond that shown by the lectin perfusion [Isolectin B4 (IB4)] and postmortem detection of perfused vessels using IB4. Injection of either N-KNA$^+$ or D-KNA$^+$ improved retinal function as assessed by ERG and OKN studies conducted pre-mortem. We also did not examine the ability of KNA$^+$ mesoderm cells to differentiate into retinal pericytes, nor did we examine epigenetic modifications in the original donor cells or in the iPSC-derived KNA$^+$ cells, which would have determined whether the programming strategy reversed the metabolic memory of longstanding diabetic disease.

In conclusion, our studies suggest that the specific mesoderm subset, KNA$^+$ cells, may be of great interest for further translation as a cell therapy. We show their protective effects on retinas of Type 2 diabetes (T2D) mice with retinal pathology, consistent with early features of human diabetic retinopathy. Both diabetic and nondiabetic sources of KNA$^+$ cells provide improvement of retinal function, structural rescue of damaged vessels with increased vascularity and perfused vessels, and restoration of aberrant signaling cascades. Future studies will focus on line-to-line comparison between those derived from diabetic versus control donors, optimization of KNA$^+$ cell concentrations, dosing intervals, and use of KNA$^+$ cells with other stem/progenitor populations to enhance their function and survival in the diseased diabetic retina. Our results provide a defined protocol for the safe, efficient, and robust derivation of hiPSC-derived specific mesoderm subset for use as a novel therapy to rescue ischemic tissues and repair blood vessels in individuals with microvascular diseases so common in diabetes (fig. S10).

MATERIALS AND METHODS

Human participants

Studies were performed according to University of Alabama (UAB) review board–approved protocol (IRB-300000173). All participants gave written informed consent. Peripheral blood samples from diabetic individuals and age- and gender-matched healthy individuals were collected at UAB Eye Clinic.

Murine studies

All animal studies were conducted in accordance with the Guidelines for the Care and Use of Laboratory Animals. All procedures were approved by the Institutional Animal Care and Use Committees (IACUCs) at Indiana University School of Medicine (IACUC protocol #10850). Male and female immunodeficient nonobese diabetic/severe combined immunodeficient (NOD/SCID) mice (6 to 12 weeks old) that were used in this study were maintained under specific pathogen–free conditions at the Indiana University Laboratory Animal Resource Center (LARC). We were also approved by the local IACUC (IACUC 20919) at UAB, Birmingham, AL, USA following guidelines stated by the Association for Research in Vision and Ophthalmology.

NHP studies

The NHP studies were performed at the Oregon Health and Science University facility. Five adult male/female macaques were used in this study. All procedures performed on the macaques were approved by IACUCs at the Oregon Health and Science University and performed in accordance with the Association for Research in Vision and Ophthalmology Statement for the use of animals in ophthalmic and vision research.

Peripheral blood mononuclear cell isolation

Peripheral blood mononuclear cells (PBMCs) were isolated from ~200 ml of blood using differential centrifugation by layering the blood on Ficoll-Paque PLUS (GE Healthcare) solution.

hiPSC generation and culture

Isolated PBMCs were stored at −80°C and shipped to ALSTEM Inc. for reprogramming into hiPSCs and for characterization. For this study, three iPSC lines derived from healthy controls (table S2A) and three hiPSC lines derived from diabetics (table S2B) were used for the in vitro and in vivo studies. The fibroblast-derived hiPSC line (DF19-9-11T) (*8*) was purchased from WiCell. hiPSCs were maintained in mTeSR1 complete medium (STEMCELL Technologies) on Matrigel (Corning) in tissue culture dishes at 37°C and 5% CO_2. Medium was changed on days 2 to 4 after hiPSCs were plated, and cells were passaged on day 5. Before cell digestion, medium was removed from the culture dish. Fresh medium with Dispase (2 mg/ml)

(Gibco) was then added to the plate. The plate was incubated at 37°C for up to 5 min until the edge of colonies were lifted from the bottom of the plate. Dispase-containing medium was aspirated, and the cells were gently washed with Dulbecco's minimum essential medium (DMEM)/F12 medium (Gibco) three times. Next, the cells on the plate were scraped with a 5-ml disposable pipette and washed with fresh medium. Cell-containing medium was centrifuged at 300*g* for 5 min, and the pellet was resuspended in complete mTeSR1 medium and was redistributed evenly in the medium. Before plating the colonies, 10-cm culture plates were precoated with Matrigel for 30 min. After the coated Matrigel was removed, 8 ml of mTeSR1 complete medium was added to the dishes, and resuspended colonies were added to the medium. The colonies were evenly distributed in the medium by shaking the plates in a multiple side-to-side motion. The morphology of the hiPSC culture was monitored as previously described (*56*).

Bulk RNA-seq studies

Human diabetic and nondiabetic iPSCs and KNA cells (four samples in total) were cultured as previously described. The cells were then detached, washed in phosphate-buffered saline (PBS), and resuspended in 200 μl of TRIzol reagent. Pure RNA was collected using the Zymogen Direct-zol RNA MiniPrep Kit (Zymo Research), and the 260/280 ratio was determined to be ≥2 for each sample. RNA quality was further assessed using a Bioanalyzer (Agilent), and all samples had a RNA Integrity Number (RIN) > 7. Complementary DNA (cDNA) generation, library preparations, and sequencing were performed by the UAB genomics core. Illumina paired-end 75–base pair sequencing was used with 25 million reads per sample. The raw sequencing data were aligned to the human reference genome (GRCh38) using Spliced Transcripts Alignment to a Reference (STAR), and quant mode was used to generate raw transcript counts. EdgeR was used to normalize the count data using trimmed mean of *M* values (TMM), and DEGs between D-/N-hiPSCs and D-/N-KNA cells were determined using the exactTest function with a square root dispersion Biased Cross-Validation (BCV) of 0.5. Spearman correlation for the four samples was done using Scanpy with three principle components. Data from this study have been uploaded to www.ncbi.nlm.nih.gov/geo/query/acc.cgi?acc=GSE191206 (Gene Expression Omnibus, accession number GSE191206).

Animal model

Mice containing a homozygous G-to-T transverse mutation in the leptin receptor (*Lepr*$^{db/db}$) display abnormal splicing and termination of the gene and loss of leptin-mediated signal transduction (*57*–*59*). These mice show a subset of T2D characteristics including obesity, hyperglycemia, and increased insulin production. Mice homozygous for the diabetes spontaneous mutation (*Lepr*^{db}) manifest morbid obesity, chronic hyperglycemia, pancreatic β cell atrophy, and become hypoinsulinemic. Obesity starts at 3 to 4 weeks of age. Elevated plasma insulin begins at 10 to 14 days and elevated blood sugar at 4 to 8 weeks. Homozygous mice are polyphagic, polydipsic, and polyuric. The *Lepr*$^{db/db}$ phenotype is influenced by the background strain on which the mutation is expressed, and two *db/db* mouse strains were used in this study. When homozygous *Lepr*$^{db/db}$ is on the C57BLKS/J genetic background (BKS.Cg-*Dock7*^{m} +/+ *Lepr*^{db}/J; stock #000642, the Jackson Laboratory), the mice are significantly and chronically hyperglycemic by 8 weeks of age. BKS.Cg-*Dock7*^{m} +/+ *Lepr*^{db}/J with blood glucose typically in the range of 250 ~ 350 mg/dl (*60*). The second strain [B6.BKS(D)-*Lepr*^{db}/J; stock #000697, the Jackson Laboratory] experiences a more severe diabetes phenotype with blood glucoses in the range of 550 to 600 mg/dl, severe depletion of insulin-producing β cells of the pancreatic islets, peripheral neuropathy, myocardial disease, and death by 10 months of age (*61*). Both T2D mouse models were purchased from the Jackson Laboratory, and, for both strains, *Lepr*$^{+/db}$ animals were used as nondiabetic controls. Body weight and nonfasting blood glucose were measured monthly, and glycated hemoglobin was measured every 3 months. Blood samples were collected from the tail of nonfasted animals, and glucose levels were determined with the glucometer system Accu-Chek Aviva Plus (Roche Diagnostic).

Directed differentiation of human pluripotent stem cells into the mesoderm (SSEA-5$^-$KNA$^+$) and ECFC (NRP-1$^+$CD31$^+$) lineages

To start differentiation, the hiPSC culture medium was switched to Stemline II medium (Sigma-Aldrich). After 2 days (day 0 of mesodermal differentiation), Activin-A (10 ng/ml; R&D Systems), FGF-2 (10 ng/ml; Stemgent), VEGF$_{165}$ (10 ng/ml; R&D Systems), and BMP4 (20 ng/ml; R&D Systems) were added to the medium for 24 hours to promote mesodermal differentiation. The next day, medium replaced with Stemline II medium containing FGF-2, VEGF$_{165}$, and BMP4. At day 3 of mesodermal differentiation, the medium was replaced with fresh Stemline II differentiation medium, and ECFC mesoderm cell sorting was performed at day 4 of mesodermal differentiation. KDR$^+$NCAM$^+$APLNR$^+$, KDR$^+$NCAM$^+$APLNR$^-$, and KDR$^+$NCAM$^-$APLNR$^-$ mesoderm fractions ± SSEA-5 depletion were sorted using flow cytometry at day 4. Sorted cells (100,000 cells/75 cm^2) from these fractions were each cultured in Matrigel-coated tissue culture flasks with fresh Stemline II medium supplemented with BMP4, VEGF$_{165}$, and FGF-2 (10 ng/ml) for additional 8 days (4 plus 8 days, total of 12 days) with fresh medium change every other day to examine for the emergence of NRP-1$^+$CD31$^+$ ECFCs as previously described (*17*).

Flow cytometry and cell sorting

Adherent cells were harvested using the TrypLE Express Enzyme (Gibco), and the cells were resuspended in the EGM-2 Endothelial Cell Growth Medium (Lonza) before staining. FcR-blocking reagent (Miltenyi Biotech) was used to prevent the nonspecific binding of antibodies. The following antibodies were used to stain the cells: anti-human SSEA-5–fluorescein isothiocyanate (FITC) (clone 8e11, STEMCELL Technologies), KDR–phycoerythrin (PE) (clone 89106, R&D Systems), NCAM-PE-Cy7 (clone NCAM16.2, BD Biosciences), APLNR-APC (Allophycocyanin) (clone 72133, R&D Systems), CD31-FITC (clone WM59, BD Pharmingen), CD144-PE (clone 16B1, eBioscience), and NRP-1–APC (clone AD5-176, Miltenyi Biotech). After the antibodies were washed using fresh medium, propidium iodide (eBioscience) was added to the cell suspension to detect dead cells. Cells were analyzed and sorted on a BD LSR 4, BD SORP Aria, or BD FACSAria (BD Biosciences). Positive cell populations were gated on the basis of fluorescent minus one controls. In some cases, sorted cells were suspended in the CryStor CS10 Freeze Media (BioLife Solutions) and stored at −80°C until use.

Flow cytometry on neural retina studies were performed in three *db/db* animals at 7 months of age and 1 month after intravitreal injection. N-KNA or D-KNA cells were injected in one eye, and saline was injected in the contralateral eye. Immediately following euthanasia, the animals were perfused with 6 ml of PBS, and the neural retinas were collected and placed in prewarmed Ringer's solution. The retinas were digested in 100 U of papain at 37°C for 30 min with flowing carbogen (95% O_2 and 5% CO_2). After digestion, the dissociation vials were placed on ice, and 4 ml of fluorescence-activated cell sorting (FACS) buffer was added to quench the papain activity. The dissociated retinas were centrifuged at 400*g* for 5 min at 4°C, the supernatant was removed and replaced with 1 ml of Ames solution, and the retinas were triturated ~30× until the retina was completely dissociated into single cells. The retinal cell suspensions were then filtered through 40-μm mesh, centrifuged, and then resuspended in 200 μl of FACS buffer containing the following primary antibodies: viability dye (LIVE/DEAD Fixable Near-IR Dead Cell Stain Kit, Invitrogen), anti-CD144 (clone: 55-7H1; BV605, BD Biosciences), and anti-CD31 (clone: MEC 13.3; BV510, BD Biosciences). After 20 min of incubation on ice, 4 ml of FACS buffer was added and the dissociated retinas were centrifuged at 400*g* for 5 min at 4°C. The supernatant was then removed and replaced with BD Cytofix/Cytoperm (BD Biosciences) for 30 min on ice. A total of 4 ml of FACS buffer was then added to each tube followed by centrifugation and resuspension in 200 ml of FACS buffer. The cells were then loaded onto the flow cytometer for analysis.

Detection of growth factor receptors on KNA$^+$ cells

The expression of cell surface receptors for growth factors and for the receptor for laminin α4 (CD146) on the KNA$^+$ population was determined by flow cytometry. The antibodies described above were used for first sorting of the KNA$^+$ cells, and then the following additional antibodies were used: CXCR4-BV421 (BioLegend), IGF1R-PE (BioLegend), CD146-BV421 (BioLegend), and PlexinB1-PE (R&D Systems). Cells were incubated for 30 min at room temperature and protected from light. After staining, the cells were centrifuged at 300*g* for 5 min at room temperature, washed, and resuspended in Stemline II medium. Flow cytometric detection of the cell surface antigens and cell sorting were performed using BD FACSCelesta (BD Biosciences).

Cell culture of ECFCs

For ECFC emergence, CD31$^+$-, CD144$^+$- or KDR$^+$-, and NRP-1$^+$-sorted cells were centrifuged at 300*g* for 5 min and then resuspended in 1:1 complete EGM-2 supplemented with 10% fetal bovine serum (GE Healthcare) and Stemline II differentiation medium. To grow ECFCs, 2500 sorted cells were plated on each well of rat tail type I collagen-coated 12-well plates. Two days after plating, the medium was replaced by three parts of EGM-2 and one part of differentiation medium. ECFC colonies with cobblestone appearance could be detected on day 7. When the cultures were confluent, ECFCs were collected and passage by replating 10,000 cells/cm^2 on collagen I–coated plates in complete EGM-2. Medium was changed every other day as described previously (*19*, *62*).

In vitro capillary network formation assay on Matrigel

Ninety-six–well plates were coated with 50 μl per well of growth factor–reduced Matrigel. After the Matrigel was solidified at 37°C for 30 min, 10,000 cells per well were added on top of Matrigel. Triplicate wells were set up for each condition. Plates were incubated overnight at 37°C for 8 to 16 hours and were monitored at ×10 magnification using a Zeiss Axiovert 25 CFL inverted microscope with a ×10 CP-ACHROMAT/0.12 numerical aperture (NA) objective. Images were taken using a SPOT RT color camera (SPOT Imaging) with the manufacturer's software.

In vivo implantation and vessel formation assay

3D cell containing collagen gel was generated using pig skin type I collagen (GeniPhys) as previously described (*63*). Briefly, to make type 1 collagen gel, ice-cold porcine skin collagen solution was mixed with 0.01 N HCl and neutralized with PBS and 0.1 N NaOH to pH 7.4. The gel (1.5 mg/ml) was kept on ice before polymerization. Cells were resuspended in the gel to reach a concentration of 4 × 10^6 cells/ml. Then, 250 μl of the cellularized gel was added to each well of a 48-well tissue culture. The plate was incubated at 37°C, in 5% CO_2 for 30 min to let the gel polymerize. Last, 500 μl of culture medium was added on the solidified gel and incubated at 37°C, in 5% CO_2 for overnight. Next, cellularized gels were picked out from the wells and implanted into the flanks of 6- to 12-week-old NOD/SCID mice as previously described (*19*). The incisions were sutured, and mice were monitored for recovery. All surgical procedures were conducted under anesthesia and constant supply of oxygen. After 2 weeks, gels were retrieved from the euthanized mice. The gels were fixed and sectioned, and then hematoxylin and eosin and human CD31 (hCD31) immunohistochemistry staining was performed to detect Human EC–derived blood vessels perfused with host red blood cells. Sections were imaged from each explant using a Leica DM 4000B microscope (Leica Microsystems) with an attached SPOT-KE digital camera (SPOT Imaging). Functional vessels that contained minimal one murine red blood cell were counted. Some sections were stained with fluorescent anti-hCD31 and anti-human NRP-1 antibodies. Olympus FV1000MPE inverted confocal/2P system was used to examine NRP-1$^+$CD31$^+$ vessels.

ECFC single-cell proliferation assay

hiPSC-derived ECFCs or mesoderm subset–derived ECs were subjected to a single-cell assay to test their clonogenic proliferative potential. Briefly, ECs were collected using the TrypLE Express Enzyme (Gibco) and resuspended in EGM-2 medium. Serial dilutions were performed to obtain a concentration of 0.68 cells in each well of collagen I–coated 96-well culture plates. The wells were checked 1 day after plating to ensure the presence of a single cell in each well. Culture medium was changed every 4 days. After 14 days, cells were stained with Sytox reagent (Invitrogen), and the number of cells in each well was counted at ×10 magnification using a Zeiss Axiovert 25 CFL inverted microscope with a ×10 CP-ACHROMAT/0.12 NA objective. Wells with different EC counts were defined as EC clusters (2 to 50 cells per well), low–proliferative potential ECFCs (51 to 500 cells per well), and HPP ECFCs (501 to 2000 and ≥2001 cells per well) as previously described (*19*, *62*).

Intravitreal injection of KNA$^+$ cells

Intravitreal injection was performed at 24 weeks of diabetes. All mice were immunosuppressed through intraperitoneal injection using cyclosporine (30 mg/kg) daily for 7 days before intravitreal injection and then biweekly for the next 3 weeks. The pupils were dilated using 1% atropine sulfate ophthalmic solution (AKORN) and 2.5% phenylephrine hydrochloride (Paragon BioTeck Inc.). Mice were anesthetized using 2.5% isoflurane (Fluriso, VetOne). A cell suspension containing 1 × 10^5 KNA$^+$ cells in 1 μl of saline was slowly injected into the vitreous cavity through the sclera/choroid using a

32-gauge beveled needle (Hamilton Company, Reno, NV) (*64*). Another cohort of mice receiving 1 μl of saline injection into the vitreous cavity was used as control. Topical triple antibiotic ointment (Allegan) was applied to the injected eye.

Optokinetic response

To evaluate the optokinetic response, a computer-based visual acuity response test (OptoMotry 1.7.7, Cerebral Mechanics) was used in all cohorts of mice. Briefly, mice were tested for visual acuity by observing their optokinetic responses to rotating sinusoidal gratings (*65*, *66*). Mice were placed on a platform at the center of a virtual reality chamber composed of four monitors that display sine wave gratings rotating at 12°/s. Mice were monitored through a video camera, which was continuously recentered on the head of the animal, and the presence or absence of the optokinetic reflex was recorded. At the beginning, mice were allowed to settle on the platform for 3 to 5 min. To assess visual acuity, initially, the grating began at a 100% contrast with spatial frequency of 0.05 cycles/deg for both directions of rotation, which gradually increased until head turning was no longer observed. Spatial frequency threshold, a measure of visual acuity, was determined automatically with the Opto-kinetic tracking (OKT) software.

Electroretinography

After overnight dark adaptation, mice were anesthetized by intramuscular injection of ketamine (85 mg/kg) (KetaVed, ketamine hydrochloride, VEDCO) and xylazine (14 mg/kg) (AnaSed LA, VetOne). Pupils were dilated using 1% atropine sulfate ophthalmic solution and 2.5% phenylephrine hydrochloride. Responses of the outer retina were recorded as previously described (*67*). Mice were placed on a temperature-regulated heating pad throughout each recording session. For the assessment of scotopic response, a stimulus intensity of 1.89 log cd-s/m^2 was presented to the dark-adapted dilated eyes in a ganzfeld (UTAS System, LKC). Measurement of scotopic a-wave amplitude was made from the prestimulus baseline to the a-wave trough. b-wave amplitude was made from the trough of the a-wave to the crest of b-wave. To evaluate the photopic response, animals were light-adapted for 5 min under a light source of 1.46 log cd-s/m^2 intensity. Afterward, photopic responses were recorded from 25 averaged flashes at 1.89 log cd-s/m^2. The amplitude of the photopic b-wave was measured from the trough of the a-wave to the crest of the b-wave. Significance was determined using one-way analysis of variance (ANOVA) and post hoc tests using Bonferroni's pairwise comparisons (GraphPad Prism 9 version 9.2.0).

Spectral domain optical coherence tomography

Pupils were dilated and then mice were anesthetized using ketamine and xylazine as described above. Each mouse was transferred to the Envisu SDOIS system (Bioptigen) for Spectral domain optical coherence tomography (SD-OCT) imaging (*68*). Eyes were then immediately covered with Systane Ultra artificial tears (Alcon Laboratories), and using an objective lens with a 50° field of view (FOV), retinal images were collected. For these images, the optic nerve was centrally positioned. The SD-OCT volumetric scans (1000 a-scans per b-scan, ×1000 b-scans per volume) were obtained within the FOV. The SDOIS system afforded a retinal FOV of ~1.5 mm, with an axial, in-depth resolution of ~6 mm. After imaging, both eyes received ophthalmic ointment to prevent corneal dehydration. During recovery, mice were placed in a heating pad warmed to 37°C until they fully recovered from general anesthesia.

Fundus imaging and fluorescein angiography

Fundus imaging and fluorescein angiography (FA) were performed using Micron IV system (Phoenix Research Laboratories) as previously described (*67*, *69*). Bright-field fundus images and fundus fluorescence images were collected from anaesthetized/dilated animals, and then the animals were injected intraperitoneally with 100 μl of 1% (w/v) fluorescein sodium (Sigma-Aldrich). FA images were captured using excitation and emission filters of 486 and 436 nm, respectively. All images were captured using StreamPix software (Norpix).

Image processing for VESGEN

db/db mice that had undergone injection with KNA$^+$ cells 1 month previously were extensively perfused with warm sterile saline and then with 0.5 cm^3 of the Griffonia Simplicifolia Lectin I (GSL I) IB4. Eyes were harvested as described above, and retinas were prepared as flat mounts. A separate cohort of mice were processed without perfusion, and the eyes were removed for processing as retinal flat mounts. Images of retinas from mice perfused with GSL I IB4 or retinas from mice stained post-mortem with GSL were processed using 2018 Photoshop Adobe Creative Cloud via a 15.6-inch Dell desktop with a recommended resolution of 1920 by 1080 pixels. Images were first prepared using the brightness/contrast tool to maximize the quality of images for tracing. A duplicate of the contrast-enhanced traced image was transformed to a binary image using the magic wand and fill tool to convert vessels to "black" and background to "white." Images were then converted to grayscale. Using a separate transparent layer, an ROI was defined and determined by the maximum vasculature area.

Vascular quantification

VESGEN is Java-based computer interactive code. VESGEN works as a plug-in feature to ImageJ software. VESGEN uses image-processing concepts of eight-neighbor pixel connectivity, skeleton, and distance map to analyze 2D, black-and-white (binary) images of vascular trees, networks, and tree-network composites. VESGEN maps typically 5 to 12 (or more) generations of vascular branching, starting from a single parent vessel. These generations are tracked and measured for critical vascular parameters that include vessel diameter, length, density and number, and tortuosity per branching generation. The impact of KNA$^+$ cell injections (experimental cohort) on vascular morphology and branching in *db/db* mice were quantified by comparing vascular parameters with *db/db* mice injected with saline (control group). For the purpose of this study, we first examined (i) changes in the number of perfused vessels, (ii) fractal dimension (Df) that characterizes the structural change from large vessels to small vessels across the retina, and (iii) total vessel length. We then examined density by three parameters vessel number density (N_v), vessel length density (L), and vessel area density (A_v), which were determined by the ROI and is defined as the proportion of the ROI occupied by vessels.

Immunocytochemistry

After been fixed with 4% (w/v) paraformaldehyde for 30 min, cells were permeabilized with 0.1% (v/v) Triton X-100 in PBS for 5 min. A total of 10% (v/v) goat serum was added, and the cells were incubated for 30 min to block unspecific antibody binding. Next, the cells were incubated with the following primary antibodies overnight at 4°C: anti-CD31 (Santa Cruz Biotechnology), anti-CD144 (eBioscience), anti–NRP-1 (Santa Cruz Biotechnology), and anti–α-SMA, (Chemicon). Then, the cells were washed with PBS three times and incubated with Alexa Fluor 488– or Alexa Fluor 565–conjugated secondary antibodies (Molecular Probe). The stained cultures were counterstaining with 4′,6-diamidino-2-phenylindole (DAPI) (DAKO). Confocal images were acquired with an Olympus FV1000MPE confocal microscope using an objective lens (UPlanSApo 60XW, NA 1.20, Olympus). Z-stack images were taken with 10-μm intervals. Images were analyzed using FV10-ASW 3.0 Viewer software (Olympus) and processed in ImageJ software.

Immunohistochemistry of murine and NHP retinas

Mice were anesthetized by intramuscular injection of ketamine/xylazine and perfused via intracardiac administration of 10 ml of 1× PBS, followed by 10 ml of 4% paraformaldehyde in PBS. Eyes were enucleated, immersion-fixed overnight in 4% paraformaldehyde in PBS at 4°C, and stored in PBS until processing. For retinal sections, eyes were placed in 30% sucrose in PBS overnight at 4°C before preparation of the frozen blocks in optimal cutting temperature embedding medium (Fisher HealthCare). Serial cross sections of retinas (20 μm) were cut and mounted on slides. Tissue sections were stored at −80°C until ready to be processed. Samples were allowed to thaw for a minimum of 1 hour at room temperature. Samples were then fixed in ice-cold acetone for 5 min and let dry for 10 min at room temperature. A 15-min permeabilization step in tris-buffered saline (TBS)–0.05% Tween 20 (TBS-T) followed. Antigen retrieval was then performed in 1× sodium citrate buffer (Vector Laboratories Inc.) for 30 min at 95°C. After a 30-min cool down step, to further reduce background staining, samples were incubated in 1% Triton X-100 in TBS for 30 min at room temperature. To block nonspecific binding, samples were incubated in 10% donkey serum in TBS for 30 min at room temperature. Following three washes in TBS-T (2 min each), retinal sections were incubated for 10 min with 3% H_2O_2 in TBS to block potential endogenous peroxidase activity. After another round of washes, tissue sections were reacted with primary antibodies overnight at 4°C: FITC-conjugated mouse anti-hCD31 (1:25; Santa Cruz Biotechnology), rat anti-mouse CD31 (1:25; BD Biosciences), or with Isolectin GS-IB4 Alexa Fluor 568 (Thermo Fisher Scientific). Following three washes in TBS-T (2 min each), retinal sections were incubated with donkey anti-rat DyLight 594 (1:250; Thermo Fisher Scientific) for 1 hour at room temperature.

The preparation of retinal flat mounts was performed as previously described (*70*, *71*). Flat mounts and/or slides were reacted with either GSL I IB4, fluorescein (1:100; Vector Laboratories Inc.) at room temperature for 4 hours or with primary antibodies overnight at 4°C: mouse anti–human nuclear antigen antibody (1:100; Abcam) (*72*–*74*) and rabbit anti–collagen IV (1:400; Abcam) (*75*). Retinas were then washed in PBS (10 min × 3) and then incubated with species-specific secondary antibodies (1:200) conjugated with either Alexa Fluor 594 (Invitrogen) or Alexa Fluor 488 (Invitrogen) for 2 hours at room temperature. After incubation with secondary antibodies, samples were extensively washed and then incubated with DAPI (Thermo Fisher Scientific) for nuclear staining for 10 min at room temperature. Last, the retinal tissue was washed with PBS and mounted with the VECTASHIELD Hardset Antifade Mounting Medium (Vector Laboratories Inc.). Digital images were acquired at the UAB High Resolution Imaging Facility core using a Zeiss microscope (Axio Imager 2, upright microscope) and a Nikon A1R confocal microscope. The system was operated by Nikon NIS Elements 5.21 software. Z-stack images were acquired at 1024 by 1024 pixel density denoised with NIS.ai algorithm and saved as 3D reconstructed files.

Gene expression analysis

Reverse transcriptase (RT) reactions were performed in the GeneAmp PCR 9700 System Thermocycler (Applied Biosystems). mRNA RT reactions were performed using the Transcriptor Univessal cDNA Master (Roche). RT reactions without templates or primer were used as controls. Gene expression levels were quantified using the ABI 7300 RT-PCR System (Applied Biosytems). Quantitative polymerase chain reaction (PCR) for mRNA was performed using FastStart Universal SYBR green master (Rox) (Roche). Reactions were performed at 95°C for 10 min, followed by 40 cycles of 95°C for 15 s and 60°C for 1 min. Relative expression levels were calculated using the comparative C_t method (*76*).

Proteomic analysis

For protein expression assays, the retina from D-KNA$^+$– and N-KNA$^+$–treated mice were disrupted in the TissueLyser LT (QIAGEN) in 200 μl of lysis buffer provided by the Functional Proteomics Reverse Phase Protein Array (RPPA) Core Facility (MD Anderson Cancer Center): 1% Triton X-100, 50 mM Hepes (pH 7.4), 150 mM NaCl, 1.5 mM $MgCl_2$, 1 mM EGTA, 100 mM NaF, 10 mM Na pyrophosphate, 1 mM Na_3VO_4, 10% glycerol, and freshly added protease and phosphatase inhibitors (Roche Diagnostics Corporation). After pelleting the debris, the protein concentration was determined with the Pierce BCA microplate procedure (Thermo Fisher Scientific) on a Synergy H1 plate reader (BioTek), adjusted to approximately 1 μg/μl and sent to RPPA Core for proteomic analysis using their standard procedures (www.mdanderson.org/research/research-resources/core-facilities/functional-proteomics-rppa-core/rppa-process.html). Data were analyzed as described for gene expression using Ingenuity Pathway Analysis (QIAGEN) (*77*). Heatmaps were created in R using the ggplot2 package per standard protocols (table S3).

Quantification and statistical analysis

All experiments were performed ≥3 times in triplicate. Results are expressed as means ± SEM. A power of analysis with a 95% confidence interval was used to calculate sample size required to obtain statistically significant results. The sampling number we used gave a normal distribution. Significance of differences was assessed by a two-tailed Student's *t* test or one-way ANOVA–Tukey post hoc test, multiple comparison test, or chi-square test. Statistical analysis was done by calculating the *P* values ($\alpha = 0.05$) using GraphPad Prism 9 version 9.2.0 (332) software. Before statistical testing, all data were assessed for divergence away from a normal (Gaussian) distribution normality test, where $P \leq 0.05$ indicates non-normal/nonparametric data. Data determined to be normally distributed will be assessed for statistical significance by a two-tailed unpaired parametric *t* test. Data determined to be non-normally distributed will be assessed for statistical significance by a two-tail Mann-Whitney nonparametric unpaired *t* test.

SUPPLEMENTARY MATERIALS

Supplementary material for this article is available at https://science.org/doi/10.1126/sciadv.abm5559

View/request a protocol for this paper from *Bio-protocol*.

REFERENCES AND NOTES

1. I. Carcamo-Orive, G. E. Hoffman, P. Cundiff, N. D. Beckmann, S. L. D'Souza, J. W. Knowles, A. Patel, D. Papatsenko, F. Abbasi, G. M. Reaven, S. Whalen, P. Lee, M. Shahbazi, M. Y. R. Henrion, K. Zhu, S. Wang, P. Roussos, E. E. Schadt, G. Pandey, R. Chang, T. Quertermous, I. Lemischka, Analysis of transcriptional variability in a large human iPSC library reveals genetic and non-genetic determinants of heterogeneity. *Cell Stem Cell* **20**, 518–532.e9 (2017).
2. T. S. Park, L. Zimmerlin, R. Evans-Moses, J. Thomas, J. S. Huo, R. Kanherkar, A. He, N. Ruzgar, R. Grebe, I. Bhutto, M. Barbato, M. A. Koldobskiy, G. Lutty, E. T. Zambidis, Vascular progenitors generated from tankyrase inhibitor-regulated naïve diabetic human iPSC potentiate efficient revascularization of ischemic retina. *Nat. Commun.* **11**, 1195 (2020).
3. I. M. Williams, J. C. Wu, Generation of endothelial cells from human pluripotent stem cells. *Arterioscler. Thromb. Vasc. Biol.* **39**, 1317–1329 (2019).
4. J. Stepniewski, N. Kachamakova-Trojanowska, D. Ogrocki, M. Szopa, M. Matlok, M. Beilharz, G. Dyduch, M. T. Malecki, A. Jozkowicz, J. Dulak, Induced pluripotent stem cells as a model for diabetes investigation. *Sci. Rep.* **5**, 8597 (2015).
5. C. E. Murry, G. Keller, Differentiation of embryonic stem cells to clinically relevant populations: Lessons from embryonic development. *Cell* **132**, 661–680 (2008).
6. K. M. Vogeli, S.-W. Jin, G. R. Martin, D. Y. R. Stainier, A common progenitor for haematopoietic and endothelial lineages in the zebrafish gastrula. *Nature* **443**, 337–339 (2006).
7. L. Dale, C. M. Jones, BMP signalling in early Xenopus development. *Bioessays* **21**, 751–760 (1999).
8. J. Yu, K. Hu, K. Smuga-Otto, S. Tian, R. Stewart, I. I. Slukvin, J. A. Thomson, Human induced pluripotent stem cells free of vector and transgene sequences. *Science* **324**, 797–801 (2009).
9. T. Era, N. Izumi, M. Hayashi, S. Tada, S. Nishikawa, S.-I. Nishikawa, Multiple mesoderm subsets give rise to endothelial cells, whereas hematopoietic cells are differentiated only from a restricted subset in embryonic stem cell differentiation culture. *Stem Cells* **26**, 401–411 (2008).
10. R. Sugimura, D. K. Jha, A. Han, C. Soria-Valles, E. L. da Rocha, Y. F. Lu, J. A. Goettel, E. Serrao, R. G. Rowe, M. Malleshaiah, I. Wong, P. Sousa, T. N. Zhu, A. Ditadi, G. Keller, A. N. Engelman, S. B. Snapper, S. Doulatov, G. Q. Daley, Haematopoietic stem and progenitor cells from human pluripotent stem cells. *Nature* **545**, 432–438 (2017).
11. G.-Y. Peng, Y. Lin, J.-J. Li, Y. Wang, H.-Y. Huang, Z.-Y. Shen, The application of induced pluripotent stem cells in pathogenesis study and gene therapy for vascular disorders: Current progress and future challenges. *Stem Cells Int.* **2019**, 9613258 (2019).
12. S. Arora, E. K. F. Yim, Y. C. Toh, Environmental specification of pluripotent stem cell derived endothelial cells toward arterial and venous subtypes. *Front. Bioeng. Biotechnol.* **7**, 143 (2019).
13. Y. Lin, C. H. Gil, M. C. Yoder, Differentiation, evaluation, and application of human induced pluripotent stem cell-derived endothelial cells. *Arterioscler. Thromb. Vasc. Biol.* **37**, 2014–2025 (2017).
14. D. T. Paik, L. Tian, J. Lee, N. Sayed, I. Y. Chen, S. Rhee, J. W. Rhee, Y. Kim, R. C. Wirka, J. W. Buikema, S. M. Wu, K. Red-Horse, T. Quertermous, J. C. Wu, Large-scale single-cell RNA-seq reveals molecular signatures of heterogeneous populations of human induced pluripotent stem cell-derived endothelial cells. *Circ. Res.* **123**, 443–450 (2018).
15. J. E. Fish, J. D. Wythe, The molecular regulation of arteriovenous specification and maintenance. *Dev. Dyn.* **244**, 391–409 (2015).
16. D. Evseenko, Y. Zhu, K. Schenke-Layland, J. Kuo, B. Latour, S. Ge, J. Scholes, G. Dravid, X. Li, W. R. MacLellan, G. M. Crooks, Mapping the first stages of mesoderm commitment during differentiation of human embryonic stem cells. *Proc. Natl. Acad. Sci. U.S.A.* **107**, 13742–13747 (2010).
17. N. Prasain, M. R. Lee, S. Vemula, J. L. Meador, M. Yoshimoto, M. J. Ferkowicz, A. Fett, M. Gupta, B. M. Rapp, M. R. Saadatzadeh, M. Ginsberg, O. Elemento, Y. Lee, S. L. Voytik-Harbin, H. M. Chung, K. S. Hong, E. Reid, C. L. O'Neill, R. J. Medina, A. W. Stitt, M. P. Murphy, S. Rafii, H. E. Broxmeyer, M. C. Yoder, Differentiation of human pluripotent stem cells to cells similar to cord-blood endothelial colony-forming cells. *Nat. Biotechnol.* **32**, 1151–1157 (2014).
18. D. A. Ingram, L. E. Mead, H. Tanaka, V. Meade, A. Fenoglio, K. Mortell, K. Pollok, M. J. Ferkowicz, D. Gilley, M. C. Yoder, Identification of a novel hierarchy of endothelial progenitor cells using human peripheral and umbilical cord blood. *Blood* **104**, 2752–2760 (2004).
19. M. C. Yoder, L. E. Mead, D. Prater, T. R. Krier, K. N. Mroueh, F. Li, R. Krasich, C. J. Temm, J. T. Prchal, D. A. Ingram, Redefining endothelial progenitor cells via clonal analysis and hematopoietic stem/progenitor cell principals. *Blood* **109**, 1801–1809 (2007).
20. G. Liao, K. Zheng, R. Shorr, D. S. Allan, Human endothelial colony-forming cells in regenerative therapy: A systematic review of controlled preclinical animal studies. *Stem Cells Transl. Med.* **9**, 1344–1352 (2020).
21. C. L. O'Neill, K. J. McLoughlin, S. E. J. Chambers, J. Guduric-Fuchs, A. W. Stitt, R. J. Medina, The vasoreparative potential of endothelial colony forming cells: A journey through pre-clinical studies. *Front. Med.* **5**, 273 (2018).
22. M. Massa, R. Campanelli, E. Bonetti, M. Ferrario, B. Marinoni, V. Rosti, Rapid and large increase of the frequency of circulating endothelial colony-forming cells (ECFCs) generating late outgrowth endothelial cells in patients with acute myocardial infarction. *Exp. Hematol.* **37**, 8–9 (2009).
23. C. J. Lyons, T. O'Brien, The functionality of endothelial-colony-forming cells from patients with diabetes mellitus. *Cells* **9**, 1731 (2020).
24. C. Tang, A. S. Lee, J. P. Volkmer, D. Sahoo, D. Nag, A. R. Mosley, M. A. Inlay, R. Ardehali, S. L. Chavez, R. R. Pera, B. Behr, J. C. Wu, I. L. Weissman, M. Drukker, An antibody against SSEA-5 glycan on human pluripotent stem cells enables removal of teratoma-forming cells. *Nat. Biotechnol.* **29**, 829–834 (2011).
25. M. E. Woodbury, T. Ikezu, Fibroblast growth factor-2 signaling in neurogenesis and neurodegeneration. *J. Neuroimmune Pharmacol.* **9**, 92–101 (2014).
26. Y. S. Hu, X. Han, X. H. Liu, STAT3: A potential drug target for tumor and inflammation. *Curr. Top. Med. Chem.* **19**, 1305–1317 (2019).
27. M. Phillipson, B. Heit, S. A. Parsons, B. Petri, S. C. Mullaly, P. Colarusso, R. M. Gower, G. Neely, S. I. Simon, P. Kubes, Vav1 is essential for mechanotactic crawling and migration of neutrophils out of the inflamed microvasculature. *J. Immunol.* **182**, 6870–6878 (2009).
28. A. J. Waskiewicz, A. Flynn, C. G. Proud, J. A. Cooper, Mitogen-activated protein kinases activate the serine/threonine kinases Mnk1 and Mnk2. *EMBO J.* **16**, 1909–1920 (1997).
29. D. A. Pulliam, S. S. Deepa, Y. Liu, S. Hill, A. L. Lin, A. Bhattacharya, Y. Shi, L. Sloane, C. Viscomi, M. Zeviani, H. Van Remmen, Complex IV-deficient Surf1$^{-/-}$ mice initiate mitochondrial stress responses. *Biochem. J.* **462**, 359–371 (2014).
30. J. L. Napoli, Cellular retinoid binding-proteins, CRBP, CRABP, FABP5: Effects on retinoid metabolism, function and related diseases. *Pharmacol. Ther.* **173**, 19–33 (2017).
31. J. E. Park, A. I. Son, R. Zhou, Roles of EphA2 in development and disease. *Genes* **4**, 334–357 (2013).
32. X. Guan, J. Lu, F. Sun, Q. Li, Y. Pang, The molecular evolution and functional divergence of lamprey programmed cell death genes. *Front. Immunol.* **10**, 1382 (2019).
33. Q. Wang, H. S. Yang, The role of Pdcd4 in tumour suppression and protein translation. *Biol. Cell* **110**, 169–177 (2018).
34. M. Lagatuz, R. J. Vyas, M. Predovic, S. Lim, N. Jacobs, M. Martinho, H. Valizadegan, D. Kao, N. Oza, C. A. Theriot, S. B. Zanello, G. Taibbi, G. Vizzeri, M. Dupont, M. B. Grant, D. J. Lindner, H. C. Reinecker, A. Pinhas, T. Y. Chui, R. B. Rosen, N. Moldovan, M. B. Vickerman, K. Radhakrishnan, P. Parsons-Wingerter, Vascular patterning as integrative readout of complex molecular and physiological signaling by VESsel GENeration analysis. *J. Vasc. Res.* **58**, 207–230 (2021).
35. R. J. Vyas, M. Young, M. C. Murray, M. Predovic, S. Lim, N. M. Jacobs, S. S. Mason, S. B. Zanello, G. Taibbi, G. Vizzeri, P. Parsons-Wingerter, Decreased vascular patterning in the retinas of astronaut crew members as new measure of ocular damage in spaceflight-associated neuro-ocular syndrome. *Invest. Ophthalmol. Vis. Sci.* **61**, 34 (2020).
36. P. Parsons-Wingerter, K. Radhakrishnan, M. B. Vickerman, P. K. Kaiser, Oscillation of angiogenesis with vascular dropout in diabetic retinopathy by VESsel GENeration analysis (VESGEN). *Invest. Ophthalmol. Vis. Sci.* **51**, 498–507 (2010).
37. H. Liu, Q. Yang, K. Radhakrishnan, D. E. Whitfield, C. L. Everhart, P. Parsons-Wingerter, S. A. Fisher, Role of VEGF and tissue hypoxia in patterning of neural and vascular cells recruited to the embryonic heart. *Dev. Dyn.* **238**, 2760–2769 (2009).
38. N. Pescosolido, A. Barbato, A. Stefanucci, G. Buomprisco, Role of electrophysiology in the early diagnosis and follow-up of diabetic retinopathy. *J. Diabetes Res.* **2015**, 319692 (2015).
39. R. Delewi, A. Andriessen, J. G. Tijssen, F. Zijlstra, J. J. Piek, A. Hirsch, Impact of intracoronary cell therapy on left ventricular function in the setting of acute myocardial infarction: A meta-analysis of randomised controlled clinical trials. *Heart* **99**, 225–232 (2013).
40. G. Ramsay, D. Cantrell, Environmental and metabolic sensors that control T cell biology. *Front. Immunol.* **6**, 99 (2015).
41. K. Ohno-Matsui, T. Uetama, T. Yoshida, M. Hayano, T. Itoh, I. Morita, M. Mochizuki, Reduced retinal angiogenesis in MMP-2-deficient mice. *Invest. Ophthalmol. Vis. Sci.* **44**, 5370–5375 (2003).
42. J. O. Lipton, M. Sahin, The neurology of mTOR. *Neuron* **84**, 275–291 (2014).
43. S. Rodriguez-Fdez, X. R. Bustelo, The Vav GEF family: An evolutionary and functional perspective. *Cells* **8**, (2019).
44. M. Kuliralo, J. Van Reck, M. Putz, A. Blero, J. Gitani, Conservative treatment of cranio-mandibular disorders, analysis of 181 cases. *Acta Stomatol. Belg.* **88**, 131–143 (1991).
45. H. Yamada, E. Yamada, N. Kwak, A. Ando, A. Suzuki, N. Esumi, D. J. Zack, P. A. Campochiaro, Cell injury unmasks a latent proangiogenic phenotype in mice with increased expression of FGF2 in the retina. *J. Cell. Physiol.* **185**, 135–142 (2000).
46. E. G. Faktorovich, R. H. Steinberg, D. Yasumura, M. T. Matthes, M. M. LaVail, Photoreceptor degeneration in inherited retinal dystrophy delayed by basic fibroblast growth factor. *Nature* **347**, 83–86 (1990).

47. Y. S. Xu, J. J. Liang, Y. Wang, X. J. Zhao, L. Xu, Y. Y. Xu, Q. C. Zou, J. M. Zhang, C. E. Tu, Y. G. Cui, W. H. Sun, C. Huang, J. H. Yang, Y. E. Chin, STAT3 undergoes acetylation-dependent mitochondrial translocation to regulate pyruvate metabolism. *Sci. Rep.* **6**, 39517 (2016).
48. S. Joshi, L. C. Platanias, Mnk kinase pathway: Cellular functions and biological outcomes. *World J. Biol. Chem.* **5**, 321–333 (2014).
49. B. Kadenbach, Regulation of cytochrome c oxidase contributes to health and optimal life. *World J. Biol. Chem.* **11**, 52–61 (2020).
50. C. Huang, W. Yuan, C. Lai, S. Zhong, C. Yang, R. Wang, L. Mao, Z. Chen, Z. Chen, EphA2-to-YAP pathway drives gastric cancer growth and therapy resistance. *Int. J. Cancer* **146**, 1937–1949 (2020).
51. Y. Duan, R. Prasad, D. Feng, E. Beli, S. Li Calzi, A. L. F. Longhini, R. Lamendella, J. L. Floyd, M. Dupont, S. K. Noothi, G. Sreejit, B. Athmanathan, J. Wright, A. R. Jensen, G. Y. Oudit, T. A. Markel, P. R. Nagareddy, A. G. Obukhov, M. B. Grant, Bone marrow-derived cells restore functional integrity of the gut epithelial and vascular barriers in a model of diabetes and ACE2 deficiency. *Circ. Res.* **125**, 969–988 (2019).
52. Y. Wang, Y. Shang, J. Li, W. Chen, G. Li, J. Wan, W. Liu, M. Zhang, Specific Eph receptor-cytoplasmic effector signaling mediated by SAM-SAM domain interactions. *eLife* **7**, e35677 (2018).
53. Y. Liu, S. Tao, L. Liao, Y. Li, H. Li, Z. Li, L. Lin, X. Wan, X. Yang, L. Chen, TRIM25 promotes the cell survival and growth of hepatocellular carcinoma through targeting Keap1-Nrf2 pathway. *Nat. Commun.* **11**, 348 (2020).
54. Z. Xu, Y. Wei, J. Gong, H. Cho, J. K. Park, E. R. Sung, H. Huang, L. Wu, C. Eberhart, J. T. Handa, Y. Du, T. S. Kern, R. Thimmulappa, A. J. Barber, S. Biswal, E. J. Duh, NRF2 plays a protective role in diabetic retinopathy in mice. *Diabetologia* **57**, 204–213 (2014).
55. J. L. Napoli, H. S. Yoo, Retinoid metabolism and functions mediated by retinoid binding-proteins. *Methods Enzymol.* **637**, 55–75 (2020).
56. H. E. Broxmeyer, M. R. Lee, G. Hangoc, S. Cooper, N. Prasain, Y. J. Kim, C. Mallett, Z. Ye, S. Witting, K. Cornetta, L. Cheng, M. C. Yoder, Hematopoietic stem/progenitor cells, generation of induced pluripotent stem cells, and isolation of endothelial progenitors from 21- to 23.5-year cryopreserved cord blood. *Blood* **117**, 4773–4777 (2011).
57. M. Barinaga, Researchers nail down leptin receptor. *Science* **271**, 913 (1996).
58. H. Chen, O. Charlat, L. A. Tartaglia, E. A. Woolf, X. Weng, S. J. Ellis, N. D. Lakey, J. Culpepper, K. J. Moore, R. E. Breitbart, G. M. Duyk, R. I. Tepper, J. P. Morgenstern, Evidence that the diabetes gene encodes the leptin receptor: Identification of a mutation in the leptin receptor gene in db/db mice. *Cell* **84**, 491–495 (1996).
59. G. H. Lee, R. Proenca, J. M. Montez, K. M. Carroll, J. G. Darvishzadeh, J. I. Lee, J. M. Friedman, Abnormal splicing of the leptin receptor in diabetic mice. *Nature* **379**, 632–635 (1996).
60. S. Konstantinides, K. Schafer, S. Koschnick, D. J. Loskutoff, Leptin-dependent platelet aggregation and arterial thrombosis suggests a mechanism for atherothrombotic disease in obesity. *J. Clin. Invest.* **108**, 1533–1540 (2001).
61. H. Kampfer, J. Paulukat, H. Muhl, C. Wetzler, J. Pfeilschifter, S. Frank, Lack of interferon-gamma production despite the presence of interleukin-18 during cutaneous wound healing. *Mol. Med.* **6**, 1016–1027 (2000).
62. D. A. Ingram, L. E. Mead, D. B. Moore, W. Woodard, A. Fenoglio, M. C. Yoder, Vessel wall-derived endothelial cells rapidly proliferate because they contain a complete hierarchy of endothelial progenitor cells. *Blood* **105**, 2783–2786 (2005).
63. P. J. Critser, S. T. Kreger, S. L. Voytik-Harbin, M. C. Yoder, Collagen matrix physical properties modulate endothelial colony forming cell-derived vessels in vivo. *Microvasc. Res.* **80**, 23–30 (2010).
64. J. M. Dominguez II, P. Hu, S. Caballero, L. Moldovan, A. Verma, G. Y. Oudit, Q. Li, M. B. Grant, Adeno-associated virus overexpression of angiotensin-converting enzyme-2 reverses diabetic retinopathy in type 1 diabetes in mice. *Am. J. Pathol.* **186**, 1688–1700 (2016).
65. G. T. Prusky, N. M. Alam, S. Beekman, R. M. Douglas, Rapid quantification of adult and developing mouse spatial vision using a virtual optomotor system. *Invest. Ophthalmol. Vis. Sci.* **45**, 4611–4616 (2004).
66. X. Qi, S. L. Pay, Y. Yan, J. Thomas Jr., A. S. Lewin, L. J. Chang, M. B. Grant, M. E. Boulton, Systemic injection of RPE65-programmed bone marrow-derived cells prevents progression of chronic retinal degeneration. *Mol. Ther.* **25**, 917–927 (2017).
67. D. Chakraborty, S. M. Conley, R. Zulliger, M. I. Naash, The K153Del PRPH2 mutation differentially impacts photoreceptor structure and function. *Hum. Mol. Genet.* **25**, 3500–3514 (2016).
68. R. S. Sulaiman, J. Quigley, X. Qi, M. N. O'Hare, M. B. Grant, M. E. Boulton, T. W. Corson, A simple optical coherence tomography quantification method for choroidal neovascularization. *J. Ocul. Pharmacol. Ther.* **31**, 447–454 (2015).
69. A. Koirala, R. S. Makkia, S. M. Conley, M. J. Cooper, M. I. Naash, S/MAR-containing DNA nanoparticles promote persistent RPE gene expression and improvement in RPE65-associated LCA. *Hum. Mol. Genet.* **22**, 1632–1642 (2013).
70. T. Chan-Ling, Glial, vascular, and neuronal cytogenesis in whole-mounted cat retina. *Microsc. Res. Tech.* **36**, 1–16 (1997).
71. A. Saadane, N. Mast, G. Trichonas, D. Chakraborty, S. Hammer, J. V. Busik, M. B. Grant, I. A. Pikuleva, Retinal vascular abnormalities and microglia activation in mice with deficiency in cytochrome P450 46A1-mediated cholesterol removal. *Am. J. Pathol.* **189**, 405–425 (2019).
72. N. Kumar, J. Richter, J. Cutts, K. T. Bush, C. Trujillo, S. K. Nigam, T. Gaasterland, D. Brafman, K. Willert, Generation of an expandable intermediate mesoderm restricted progenitor cell line from human pluripotent stem cells. *eLife* **4**, e08413 (2015).
73. W. Li, K. Li, J. Gao, Z. Yang, Autophagy is required for human umbilical cord mesenchymal stem cells to improve spatial working memory in APP/PS1 transgenic mouse model. *Stem Cell Res. Ther.* **9**, 9 (2018).
74. K. Ogawa, H. Suga, C. Ozone, M. Sakakibara, T. Yamada, M. Kano, K. Mitsumoto, T. Kasai, Y. Kodani, H. Nagasaki, N. Yamamoto, D. Hagiwara, M. Goto, R. Banno, Y. Sugimura, H. Arima, Vasopressin-secreting neurons derived from human embryonic stem cells through specific induction of dorsal hypothalamic progenitors. *Sci. Rep.* **8**, 3615 (2018).
75. H. Chakravarthy, E. Beli, S. Navitskaya, S. O'Reilly, Q. Wang, N. Kady, C. Huang, M. B. Grant, J. V. Busik, Imbalances in mobilization and activation of pro-inflammatory and vascular reparative bone marrow-derived cells in diabetic retinopathy. *PLOS ONE* **11**, e0146829 (2016).
76. T. L. McKay, D. J. Gedeon, M. B. Vickerman, A. G. Hylton, D. Ribita, H. H. Olar, P. K. Kaiser, P. Parsons-Wingerter, Selective inhibition of angiogenesis in small blood vessels and decrease in vessel diameter throughout the vascular tree by triamcinolone acetonide. *Invest. Ophthalmol. Vis. Sci.* **49**, 1184–1190 (2008).
77. S. Li Calzi, L. C. Shaw, L. Moldovan, W. C. Shelley, X. Qi, L. Racette, J. L. Quigley, S. D. Fortmann, M. E. Boulton, M. C. Yoder, M. B. Grant, Progenitor cell combination normalizes retinal vascular development in the oxygen-induced retinopathy (OIR) model. *JCI Insight* **4**, e129224 (2019).

Acknowledgments: We would like to acknowledge B. Asare-Bediako and Y. Adu Agyeiwaah for technical help. M. Gorbatyuk and T. W. Kraft (School of Optometry, UAB) provided LKC for ERG and OptoMotry for visual acuity study, respectively. In addition, we thank the members of the Indiana University Melvin and Bren Simon Cancer Center Flow Cytometry Resource Facility (FCRF) for outstanding technical support. This work was supported in part by Riley Children's Foundation. In addition, we thank Indiana University School of Medicine LARC. This paper is dedicated to the memory of G. Lutty who pioneered the use of iPSCs for retinal repair and who was a trusted and loved colleague. **Funding:** The vision core (S10 RR026887) provides Micron IV for fundus study, and the funding source came from NEI [EY012601 (to M.B.G.)]. Research reported in this publication was supported by the UAB High Resolution Imaging Facility and by VSRC core grant P30 EY003039. Microscopy was also conducted at the Indiana Center for Biological Microscopy. The Indiana University Melvin and Bren Simon Cancer Center FCRF is funded, in part, by NIH, National Cancer Institute (NCI) grant P30 CA082709 and National Institute of Diabetes and Digestive and Kidney Diseases (NIDDK) grant U54 DK106846. The FCRF is supported, in part, by NIH instrumentation grant 1S10D012270. D.N.K. was supported by NIH grants U01TR001810, R01HL095993, and N01 75N92020C00005. M.P.M. was supported by National Heart, Lung, and Blood Institute (NHLBI) grant R01HL128827-01. **Author contributions:** Conceptualization: C.-H.G., D.C., N.P., M.C.Y., M.E.B., and M.B.G. Methodology: C.-H.G., D.C., N.P., K.B., Y.L., H.-M.C., M.C.Y., and M.B.G. Investigation: C.-H.G., D.C., C.P.V., N.P., S.L.C., S.D.F., P.H., C.H., M.S.S., Y.L., X.H., M.D.D., J.L.F., R.P., A.L.F.L., T.J.M., M.E.B., M.J., and D.N.K. Writing—Original draft: C.-H.G., D.C., N.P., M.C.Y., and M.B.G. Writing—Review and editing: C.-H.G., D.C., D.N.K., M.E.B., M.C.Y., and M.B.G. Funding acquisition: M.E.B., D.N.K., M.P.M., M.C.Y., and M.B.G. Supervision: M.C.Y. and M.B.G. **Competing interests:** M.C.Y. and N.P. are inventors on a pending patent US20190211304A1 related to this work filed by Indiana University Research and Technology Corp (no. 16/323,722, filed 4 August 2017, published 11 July 2019). M.C.Y. is the scientific founder and holds equity in Vascugen Inc., a biotechnology company deriving regenerative medicine cell therapies from iPSCs. The authors declare that they have no other competing interests. **Data and materials availability:** All data needed to evaluate the conclusions in the paper are present in the paper and/or the Supplementary Materials.

Submitted 25 September 2021
Accepted 11 January 2022
Published 4 March 2022
10.1126/sciadv.abm5559